arXiv:1608.06721v1 [math.NA] 24 Aug 2016

A Newton multigrid method for steady-state shallow water equations with topography and dry areas

Kailiang Wu, Huazhong Tang [1]

HEDPS, CAPT & LMAM, School of Mathematical Sciences, Peking University, Beijing 100871, P.R. China

Abstract

The paper develops a Newton multigrid (MG) method for one- and two-dimensional steady-state shallow water equations (SWEs) with topography and dry areas. It solves the nonlinear system arising from the well-balanced finite volume discretization of the steady-state SWEs by using Newton's method as the outer iteration and a geometric MG method with the block symmetric Gauss-Seidel smoother as the inner iteration. The proposed Newton MG method makes use of the local residual to regularize the Jacobian matrix of the Newton iteration, and can handle the steady-state problem with wet/dry transitions. Several numerical experiments are conducted to demonstrate the efficiency, robustness, and well-balanced property of the proposed method. The relation between the convergence behavior of the Newton MG method and the distribution of the eigenvalues of the iteration matrix is detailedly discussed.

Key words: Newton's method, multigrid, block symmetric Gauss-Seidel, shallow water equations, steady-state solution.
2010 Mathematics Subject Classification: 65N22, 65N08, 65N55

1 Introduction

The shallow water equations (SWEs) are commonly used to describe the motion of "shallow" free-surface flows subject to gravitational force and have played a critical role in the modeling and simulation of the flows in rivers or channels, the ocean tides, and the

Email addresses: wukl@pku.edu.cn (Kailiang Wu), hztang@math.pku.edu.cn (Huazhong Tang).
[1] Corresponding author. Tel: +86-10-62757018; Fax: +86-10-62751801.

tsunami, etc. Under the assumption of incompressible fluid and hydrostatic pressure distribution, with the vertical acceleration of water particles neglected, the SWEs may be derived by depth-integrating the Navier-Stokes equations as follows [1]

$$\frac{\partial \boldsymbol{U}}{\partial t} + \nabla \cdot \boldsymbol{F}(\boldsymbol{U}) = \boldsymbol{S}(\boldsymbol{x}, \boldsymbol{U}), \tag{1.1}$$

where t denotes time, and the effect of bed slope on the flow has been modeled by the inclusion of source terms at the right hand side of (1.1) which modifies the momentum equations. In the 2D Cartesian coordinates $\boldsymbol{x} = (x, y)$, the conservative vector $\boldsymbol{U}$, the flux vector $\boldsymbol{F} = (\boldsymbol{F}_1, \boldsymbol{F}_2)$, and the source term $\boldsymbol{S}$ in (1.1) are given by

$$\boldsymbol{U} = \begin{pmatrix} h \\ h\boldsymbol{u}^{\mathrm{T}} \end{pmatrix}, \quad \boldsymbol{F} = \begin{pmatrix} h\boldsymbol{u} \\ h\boldsymbol{u}^{\mathrm{T}}\boldsymbol{u} + \frac{1}{2}gh^2\boldsymbol{I} \end{pmatrix}, \quad \boldsymbol{S} = \begin{pmatrix} 0 \\ -gh\nabla z \end{pmatrix},$$

in which $\boldsymbol{u} = (u, v)$ denotes the velocity vector, g is the acceleration due to gravity, $\boldsymbol{I}$ is the identity matrix, and h is the water depth, i.e. the height of water above the riverbed topography $z(\boldsymbol{x})$. Dropping the time derivatives in (1.1) gives the the steady-state SWEs

$$\nabla \cdot \boldsymbol{F}(\boldsymbol{U}) = \boldsymbol{S}(\boldsymbol{x}, \boldsymbol{U}). \tag{1.2}$$

If the water is at rest, i.e. $\boldsymbol{u}(\boldsymbol{x}) = \boldsymbol{0}$, then the momentum parts in the above equations reduce to

$$\frac{1}{2}(gh^2)_x = -ghz_x, \quad \frac{1}{2}(gh^2)_y = -ghz_y, \tag{1.3}$$

which imply the so-called well-balanced property, i.e. "steady state of the water at rest"

$$\boldsymbol{u}(\boldsymbol{x}) = \boldsymbol{0}, \quad h(\boldsymbol{x}) + z(\boldsymbol{x}) = \text{const.}$$

Up to now, there exist various numerical methods for the SWEs, such as the finite difference scheme based on flux-difference splitting [2], the generalized Riemann problem scheme [3], high-order WENO schemes [4,5], the gas-kinetic schemes [6,7], the moving mesh method [8], and the Runge-Kutta discontinuous Galerkin methods [9,10], and so on. Most of them are explicit for the time-dependent SWEs, and can successfully simulate the evolution of the time-dependent solutions with good accuracy in time. If using the explicit time advancing method to investigate the steady-state behavior of the flow, then the long time simulation is needed and becomes time-consuming due to the small time step size satisfying a Courant-Friedrichs-Lewy condition to guarantee stability. For example, in the sediment transport and morphodynamic change model [11,12], the time stiffness arising from the characteristic time scales in flow and sediment transport seriously challenges the long time simulation if the interaction of water flow with bed topography is very weak. For such case, the implicit or semi-implicit schemes are attractive, such as the multigrid semi-implicit finite difference method [13], the linearized implicit scheme with a modified Roe flux [11], the space-time discontinuous residual distribution scheme [14], the implicit higher-order compact scheme [15], and the semi-implicit discontinuous Galerkin methods [16,17] etc. In fact, the time step size for an implicit scheme is also often constrained

by convergence. Even for the same time step size as used in the explicit case, unsteady solutions of the implicit schemes may be less accurate. An implicit scheme usually requires solving a nonlinear equation by some iteration method, and thus it is also very time-consuming. For the steady-state behavior of the SWEs flow, another way is to directly solve the steady-state SWEs, see e.g. [18], and thus developing robust and efficient solver for corresponding nonlinear algebraic system is key. Unfortunately there are few such study for the steady-state SWEs, but the steady-state Euler equations and Navier-Stokes equations have been well solved numerically, see e.g. [19,20,21,22,23]. For example, a multigrid block lower-upper symmetric Gauss-Seidel (LU-SGS) algorithm was proposed for the 2D steady-state Euler equations on unstructured grid [22]. Unlike the existing methods which add the pseudo-time terms to the steady-state equations, the norm of the local residual in each cell was used to regularize the nonlinear algebraic system arising from the spatial discretization of the steady-state Euler equations. The Newton iteration was then adopted to solve the nonlinear algebraic system and the multigrid method was used as the inner iteration with the BLU-SGS smoother.

The aim of the paper is to extend the Newton multigrid method [22] to the steady-state SWEs and investigate its convergence, in which the steady-state SWEs are discretized by a well-balanced hydrostatic reconstruction, the wet/dry transition is numerically handled, the resulting nonlinear algebraic system is iteratively solved by using the Newton multigrid iteration, and convergence behavior of the method for different numerical fluxes is detailedly investigated in numerical experiments through the distribution of the eigenvalues of the iteration matrix. The paper is organized as follows. Section 2 presents the Newton multigrid method, including the well-balanced spatial discretization of the steady-state SWEs in Subsection 2.1, the regularization of the resulting nonlinear system and its Newton iteration linearization in Subsection 2.2, the geometric multigrid method in Subsection 2.3, and the solution procedure of the Newton multigrid method in Subsection 2.4. Section 3 conducts several numerical experiments to demonstrate the efficiency and robustness of the proposed Newton multigrid method and presents a detailed discussion on the relation between the convergence behavior of the proposed method and the distribution of the eigenvalues of the block symmetric Gauss-Seidel iteration matrix for different numerical fluxes. Section 4 concludes the paper with several remarks.

2 Numerical method

This section is devoted to present the Newton multigrid method for steady-state SWEs (1.2). Let $\mathcal{T}$ be a partition of the spatial domain Ω_p, and $\mathcal{K}_i \in \mathcal{T}$ be the ith cell, whose centroid is $\boldsymbol{x}_i$. Use $\partial\mathcal{K}_i$ to denote the edge set of $\mathcal{K}_i$, e_{ij} to be the edge of $\mathcal{K}_i$ sharing with the neighboring cell $\mathcal{K}_j$, i.e. $e_{ij} = \partial\mathcal{K}_i \cap \partial\mathcal{K}_j$, $\boldsymbol{n}_{ij} = (n_{ij}^x, n_{ij}^y)^{\mathrm{T}}$ to be the unit normal vector of e_{ij}, pointing from $\mathcal{K}_i$ to $\mathcal{K}_j$, and $|e_{ij}|$ to denote the length of edge e_{ij}.

2.1 Well-balanced finite volume discretization

This section presents the well-balanced finite volume discretization of the steady-state SWEs (1.2). Integrating (1.2) over the cell $\mathcal{K}_i$ and using the divergence theorem give

$$\sum_{e_{ij}\in\partial\mathcal{K}_i}\int_{e_{ij}}\boldsymbol{F}_{\boldsymbol{n}_{ij}}(\boldsymbol{U})\,\mathrm{d}S=\iint_{\mathcal{K}_i}\boldsymbol{S}(\boldsymbol{x},\boldsymbol{U})\,\mathrm{d}\boldsymbol{x}, \tag{2.1}$$

where $\boldsymbol{F}_{\boldsymbol{n}_{ij}}(\boldsymbol{U}):=\boldsymbol{F}(\boldsymbol{U})\cdot\boldsymbol{n}_{ij}$. If let $\boldsymbol{u}=\boldsymbol{0}$, then (2.1) reduces to

$$\sum_{e_{ij}\in\partial\mathcal{K}_i}\int_{e_{ij}}\boldsymbol{S}_{ij}(h)\,\mathrm{d}S:=\sum_{e_{ij}\in\partial\mathcal{K}_i}\int_{e_{ij}}\frac{1}{2}gh^2\widetilde{\boldsymbol{n}}_{ij}\,\mathrm{d}S=\iint_{\mathcal{K}_i}\boldsymbol{S}(\boldsymbol{x},\boldsymbol{U})\,\mathrm{d}\boldsymbol{x}, \tag{2.2}$$

where $\widetilde{\boldsymbol{n}}_{ij}=(0,n_{ij}^x,n_{ij}^y)^{\mathrm{T}}$. It is a starting point of the hydrostatic reconstruction method [24] to derive a well-balanced method.

Reconstruct a piecewise polynomial $\boldsymbol{U}_h(\boldsymbol{x})$ to approximate the solution $\boldsymbol{U}(\boldsymbol{x})$, e.g.

$$\boldsymbol{U}_h(\boldsymbol{x})=\overline{\boldsymbol{U}}_i,\quad\forall\boldsymbol{x}\in\mathcal{K}_i, \tag{2.3}$$

where $\overline{\boldsymbol{U}}_i$ is the cell average approximation of $\boldsymbol{U}(\boldsymbol{x})$ over $\mathcal{K}_i$. Replacing $\boldsymbol{U}(\boldsymbol{x})$ in (2.1) with $\boldsymbol{U}_h(\boldsymbol{x})$, using the midpoint quadrature to evaluate the integral, and approximating the values of $\boldsymbol{F}_{n_{ij}}(\boldsymbol{U})$ and $\boldsymbol{S}_{ij}(h)$ at the midpoint $\boldsymbol{x}_{e_{ij}}$ of the edge e_{ij} by numerical fluxes give the finite volume discretization of (1.2) as follows

$$\sum_{e_{ij}\in\partial\mathcal{K}_i}|e_{ij}|\,\widehat{\boldsymbol{\mathcal{F}}}\left(\overline{\boldsymbol{U}}_i,\overline{\boldsymbol{U}}_j,z_i,z_j\right)=\boldsymbol{0}, \tag{2.4}$$

with

$$\widehat{\boldsymbol{\mathcal{F}}}\left(\overline{\boldsymbol{U}}_i,\overline{\boldsymbol{U}}_j,z_i,z_j\right):=\widehat{\boldsymbol{F}}_{\boldsymbol{n}_{ij}}\left(\boldsymbol{U}_{e_{ij},-},\boldsymbol{U}_{e_{ij},+}\right)-\boldsymbol{S}_{ij}\left(\hat{h}_{e_{ij},-}\right), \tag{2.5}$$

where $\boldsymbol{U}_{e_{ij},\pm}=:\left(h_{e_{ij},-},h_{e_{ij},-}\boldsymbol{u}_{e_{ij},-}\right)^{\mathrm{T}}$ denote the left and right limit values of $\boldsymbol{U}_h(\boldsymbol{x})$ at the point $\boldsymbol{x}_{e_{ij}}$ in the direction $\boldsymbol{n}_{ij}$, $\widehat{\boldsymbol{F}}_{n_{ij}}\left(\boldsymbol{U}_{e_{ij},-},\boldsymbol{U}_{e_{ij},+}\right)$ is any given numerical flux satisfying the consistency

$$\widehat{\boldsymbol{F}}_{\boldsymbol{n}_{ij}}\left(\boldsymbol{U},\boldsymbol{U}\right)=\boldsymbol{F}_{n_{ij}}\left(\boldsymbol{U}\right),$$

$$\boldsymbol{S}_{ij}\left(\hat{h}_{e_{ij},-}\right)=\left(0,n_{ij}^x\frac{g}{2}h_{e_{ij},-}^2,n_{ij}^y\frac{g}{2}h_{e_{ij},-}^2\right)^{\mathrm{T}},$$

and

$$\begin{aligned}h_{e_{ij},-}&=\max\left\{0,\bar{h}_i+z_i-\max\{z_i,z_j\}\right\},\quad\boldsymbol{u}_{e_{ij},-}=\bar{\boldsymbol{u}}_i,\\h_{e_{ij},+}&=\max\left\{0,\bar{h}_j+z_j-\max\{z_i,z_j\}\right\},\quad\boldsymbol{u}_{e_{ij},+}=\bar{\boldsymbol{u}}_j.\end{aligned} \tag{2.6}$$

Such locally reconstructed heights can roughly capture dry regions where $h=0$, see [24] for a more detailed discussion.

Remark 2.1 *For 1D steady-state SWEs, first-order accurate well-balanced scheme may be described as follows*

$$\hat{\boldsymbol{F}}_{i+\frac{1}{2}} - \hat{\boldsymbol{F}}_{i-\frac{1}{2}} = \boldsymbol{S}_i, \tag{2.7}$$

where numerical flux $\hat{\boldsymbol{F}}_{i+\frac{1}{2}}$ *and source term* $\boldsymbol{S}_i$ *are*

$$\hat{\boldsymbol{F}}_{i+\frac{1}{2}} = \hat{\boldsymbol{F}}(\boldsymbol{U}_{i+\frac{1}{2},-}, \boldsymbol{U}_{i+\frac{1}{2},+}), \quad \boldsymbol{S}_i = \left(0, \frac{g}{2}(h^2_{i+\frac{1}{2},-} - h^2_{i-\frac{1}{2},+})\right)^{\mathrm{T}}. \tag{2.8}$$

and the left and right limits of the approximate solution at $x_{i+\frac{1}{2}}$ *are*

$$\begin{aligned} h_{i+\frac{1}{2},-} &= \max\left\{0, \bar{h}_i + z_i - \max\{z_i, z_{i+1}\}\right\}, & u_{i+\frac{1}{2},-} &= \bar{u}_i, \\ h_{i+\frac{1}{2},+} &= \max\left\{0, \bar{h}_{i+1} + z_{i+1} - \max\{z_i, z_{i+1}\}\right\}, & u_{i+\frac{1}{2},+} &= \bar{u}_{i+1}. \end{aligned} \tag{2.9}$$

Remark 2.2 *Three numerical fluxes will be considered in this work. The first is the HLLC (resp. HLL) flux for 2D (resp. 1D) SWEs, see [25,26]. The 2D HLL flux is defined by*

$$\begin{aligned} &\widehat{\boldsymbol{F}}^{HLL}_{\boldsymbol{n}_{ij}}\left(\boldsymbol{U}_{e_{ij},-}, \boldsymbol{U}_{e_{ij},+}\right) \\ &= \begin{cases} \boldsymbol{F}_{\boldsymbol{n}_{ij}}\left(\boldsymbol{U}_{e_{ij},-}\right), & s_L \geq 0, \\ \dfrac{s_R \boldsymbol{F}_{\boldsymbol{n}_{ij}}\left(\boldsymbol{U}_{e_{ij},-}\right) - s_L \boldsymbol{F}_{\boldsymbol{n}_{ij}}\left(\boldsymbol{U}_{e_{ij},+}\right) + s_L s_R\left(\boldsymbol{U}_{e_{ij},+} - \boldsymbol{U}_{e_{ij},-}\right)}{s_R - s_L}, & s_L < 0 < s_R, \\ \boldsymbol{F}_{\boldsymbol{n}_{ij}}\left(\boldsymbol{U}_{e_{ij},+}\right), & s_R \leq 0, \end{cases} \end{aligned} \tag{2.10}$$

where

$$s_L = \begin{cases} u_{n_{ij},+} - 2\sqrt{g h_{e_{ij},+}}, & h_{e_{ij},-} = 0, \\ \min\left\{u_{n_{ij},-} - \sqrt{g h_{e_{ij},-}}, u_{n_{ij},*} - \sqrt{g h_{e_{ij},*}}\right\}, & h_{e_{ij},-} \neq 0, \end{cases}$$

and

$$s_R = \begin{cases} u_{n_{ij},-} + 2\sqrt{g h_{e_{ij},-}}, & h_{e_{ij},+} = 0, \\ \max\left\{u_{n_{ij},+} + \sqrt{g h_{e_{ij},+}}, u_{n_{ij},*} + \sqrt{g h_{e_{ij},*}}\right\}, & h_{e_{ij},+} \neq 0, \end{cases}$$

here $u_{n_{ij},\pm} := \boldsymbol{u}_{e_{ij},\pm} \cdot \boldsymbol{n}_{ij}$, *and*

$$\begin{aligned} u_{n_{ij},*} &= \frac{u_{n_{ij},-} + u_{n_{ij},+}}{2} + \sqrt{g h_{e_{ij},-}} - \sqrt{g h_{e_{ij},+}}, \\ h_{e_{ij},*} &= \frac{1}{4g}\left[\sqrt{g h_{e_{ij},-}} + \sqrt{g h_{e_{ij},+}} + \frac{u_{n_{ij},-} - u_{n_{ij},+}}{2}\right]^2. \end{aligned}$$

Based on the rotational invariance property of 2D SWEs [27]

$$\boldsymbol{T}_{n_{ij}} \widehat{\boldsymbol{F}}^{HLL}_{\boldsymbol{n}_{ij}}\left(\boldsymbol{U}_{e_{ij},-}, \boldsymbol{U}_{e_{ij},+}\right) = \widehat{\boldsymbol{F}}^{HLL}_{1}\left(\boldsymbol{T}_{\boldsymbol{n}_{ij}} \boldsymbol{U}_{e_{ij},-}, \boldsymbol{T}_{\boldsymbol{n}_{ij}} \boldsymbol{U}_{e_{ij},+}\right) =: \left(\widehat{f}_1, \widehat{f}_2, \widehat{f}_3\right)^{\mathrm{T}},$$

with

$$\boldsymbol{T}_{\boldsymbol{n}_{ij}} = \begin{pmatrix} 1 & 0 & 0 \\ 0 & n_{ij}^x & n_{ij}^y \\ 0 & -n_{ij}^y & n_{ij}^x \end{pmatrix},$$

the HLLC flux may be given by

$$\widehat{\boldsymbol{F}}_{\boldsymbol{n}_{ij}}^{HLLC}\left(\boldsymbol{U}_{e_{ij},-}, \boldsymbol{U}_{e_{ij},+}\right) = \boldsymbol{T}_{\boldsymbol{n}_{ij}}^{-1} \widehat{\boldsymbol{F}}_{1}^{HLLC}\left(\boldsymbol{T}_{\boldsymbol{n}_{ij}}\boldsymbol{U}_{e_{ij},-}, \boldsymbol{T}_{\boldsymbol{n}_{ij}}\boldsymbol{U}_{e_{ij},+}\right),$$

where

$$\widehat{\boldsymbol{F}}_{1}^{HLLC}\left(\boldsymbol{T}_{\boldsymbol{n}_{ij}}\boldsymbol{U}_{e_{ij},-}, \boldsymbol{T}_{\boldsymbol{n}_{ij}}\boldsymbol{U}_{e_{ij},+}\right) = \begin{cases} \left(\widehat{f}_1, \widehat{f}_2, \widehat{f}_3\right)^{\mathrm{T}}, & s_L \geq 0 \ \text{or}\ s_R \leq 0, \\ \left(\widehat{f}_1, \widehat{f}_2, u_{\tau_{ij},-}\widehat{f}_1\right)^{\mathrm{T}}, & s_L < 0 \leq s_M, \\ \left(\widehat{f}_1, \widehat{f}_2, u_{\tau_{ij},+}\widehat{f}_1\right)^{\mathrm{T}}, & s_M < 0 < s_R, \end{cases}$$

with

$$u_{\tau_{ij},\pm} := -u_{e_{ij},\pm} n_{ij}^y + v_{e_{ij},\pm} n_{ij}^x,$$

and

$$s_M := \frac{s_L h_{e_{ij},+}\left(u_{n_{ij},+} - s_R\right) - s_R h_{e_{ij},-}\left(u_{n_{ij},-} - s_L\right)}{h_{e_{ij},+}\left(u_{n_{ij},+} - s_R\right) - h_{e_{ij},-}\left(u_{n_{ij},-} - s_L\right)}.$$

The second is the local Lax-Friedrichs (LLF) flux

$$\widehat{\boldsymbol{F}}_{\boldsymbol{n}_{ij}}^{LLF}\left(\boldsymbol{U}_{e_{ij},-}, \boldsymbol{U}_{e_{ij},+}\right) = \frac{1}{2}\Big(\boldsymbol{F}_{\boldsymbol{n}_{ij}}(\boldsymbol{U}_{e_{ij},-}) + \boldsymbol{F}_{\boldsymbol{n}_{ij}}(\boldsymbol{U}_{e_{ij},+}) - s_{\max}(\boldsymbol{U}_{e_{ij},+} - \boldsymbol{U}_{e_{ij},-})\Big), \quad (2.11)$$

where $s_{\max}$ denotes an estimation of the fastest wave speed in the local 1D Riemann problem solution, and is usually taken as an upper bound for the absolute value of eigenvalues of the Jacobian $\partial \boldsymbol{F}_{n_{ij}}/\partial \boldsymbol{U}$ as follows

$$s_{\max} = \max\left\{|u_{n_{ij},-}| + \sqrt{g h_{e_{ij},-}}, |u_{n_{ij},+}| + \sqrt{g h_{e_{ij},+}}\right\}.$$

If there exist wet/dry transitions, then because the speed of a wet/dry front is of form $S_{*+} = u_{n_{ij},+} - 2\sqrt{g h_{e_{ij},+}}$ for a left dry state and $S_{*-} = u_{n_{ij},-} + 2\sqrt{g h_{e_{ij},-}}$ for a right dry state [28], $s_{\max}$ should be appropriately larger in the presence of wet/dry fronts to avoid numerical instabilities and taken as follows

$$s_{\max} = \max\left\{|u_{n_{ij},-}| + \sqrt{g h_{e_{ij},-}}, |u_{n_{ij},+}| + \sqrt{g h_{e_{ij},+}}\right\} + \varepsilon_r \sqrt{g \max\left\{h_{e_{ij},-}, h_{e_{ij},+}\right\}},$$

where $\varepsilon_r = 0.03$ in our computations.

The third is the Roe flux with Harten's entropy fix

$$\widehat{\boldsymbol{F}}_{\boldsymbol{n}_{ij}}^{Roe}\left(\boldsymbol{U}_{e_{ij},-}, \boldsymbol{U}_{e_{ij},+}\right) = \frac{1}{2}\Big(\boldsymbol{F}_{\boldsymbol{n}_{ij}}(\boldsymbol{U}_{e_{ij},-}) + \boldsymbol{F}_{\boldsymbol{n}_{ij}}(\boldsymbol{U}_{e_{ij},+}) - \sum_{k=1}^{m} Q\left(\widehat{\lambda}_k\right)\widehat{\chi}_k \widehat{\boldsymbol{r}}_k\Big), \quad (2.12)$$

where m is equal to 2 (resp. 3) for the 1D (resp. 2D) case, $\widehat{\lambda}_k = \widehat{\lambda}_k(\boldsymbol{U}_{e_{ij},-}, \boldsymbol{U}_{e_{ij},+})$ and $\widehat{\boldsymbol{r}}_k = \widehat{\boldsymbol{r}}_k(\boldsymbol{U}_{e_{ij},-}, \boldsymbol{U}_{e_{ij},+})$ are the eigenvalues and corresponding right eigenvectors of the Roe matrix, respectively, $\widehat{\chi}_k$ solves the system

$$\boldsymbol{U}_{e_{ij},+} - \boldsymbol{U}_{e_{ij},-} = \sum_{k=1}^{m} \widehat{\chi}_k \widehat{\boldsymbol{r}}_k,$$

and

$$Q(x) = \begin{cases} \frac{x^2}{4\varepsilon_f} + \varepsilon_f, & |x| < 2\varepsilon_f, \\ |x|, & |x| \geq 2\varepsilon_f, \end{cases}$$

where ε_f is a small positive constant, e.g. 0.4 in later computations.

Remark 2.3 *Let us discuss the boundary conditions for the discrete problem (2.4). If the boundary is open, according to the local Froude number $F_r := |\boldsymbol{u}|/\sqrt{gh}$, the numerical boundary conditions are specified as follows:*

- *Subcritical inflow boundary $\{F_r < 1, u_n < 0\}$: $\mathcal{R}_{\mathrm{g}}^- = \mathcal{R}_I^-$, and $h_{\mathrm{g}} u_{n,\mathrm{g}}$ and $u_{\tau,\mathrm{g}}$ are prescribed.*
- *Subcritical outflow boundary $\{F_r < 1, u_n > 0\}$: $\mathcal{R}_{\mathrm{g}}^- = \mathcal{R}_I^-$, $u_{\tau,\mathrm{g}} = u_{\tau,I}$, and h_{g} is prescribed.*
- *Supercritical inflow boundary $\{F_r > 1, u_n < 0\}$: h_{g}, $u_{n,\mathrm{g}}$, and $u_{\tau,\mathrm{g}}$ are prescribed.*
- *Supercritical outflow boundary $\{F_r > 1, u_n > 0\}$: $h_{\mathrm{g}} = h_I$, $u_{n,\mathrm{g}} = u_{n,I}$, and $u_{\tau,\mathrm{g}} = u_{\tau,I}$.*

Here $\mathcal{R}^{\mp} := u_n \pm 2\sqrt{gh}$ denotes 1D Riemann invariant associated with the eigenvalues $u_n \mp \sqrt{gh}$, u_n and u_τ are the normal and tangential velocity components to the cell interface located on the domain boundary, respectively. The quantities with subscripts g *and I denote the values from the ghost and interior cells adjacent to the domain boundary, respectively.*

The slip boundary conditions $\{h_{\mathrm{g}} = h_I, u_{n,\mathrm{g}} = 0$, and $u_{\tau,\mathrm{g}} = u_{\tau,I}\}$ or the reflective boundary conditions $\{h_{\mathrm{g}} = h_I$, $u_{n,\mathrm{g}} = -u_{n,I}$, and $u_{\tau,\mathrm{g}} = u_{\tau,I}\}$ may be specified on the wall.

2.2 Newton's iterative method

As soon as the boundary conditions are specified, the approximate solutions of the SWEs (1.2) may be obtained by iteratively solving the nonlinear algebraic system (2.4) with respect to the unknown variables $\overline{\boldsymbol{U}}_i$. Here Newton's iteration method is employed to solve (2.4) with the formula

$$\sum_{e_{ij} \in \partial \mathcal{K}_i} |e_{ij}| \left(\frac{\partial \widehat{\boldsymbol{\mathcal{F}}}}{\partial \overline{\boldsymbol{U}}_i} \right)_{ij}^{(n)} \delta \boldsymbol{U}_i^{(n)} + \sum_{e_{ij} \in \partial \mathcal{K}_i} |e_{ij}| \left(\frac{\partial \widehat{\boldsymbol{\mathcal{F}}}}{\partial \overline{\boldsymbol{U}}_j} \right)_{ij}^{(n)} \delta \boldsymbol{U}_j^{(n)} = -\boldsymbol{R}_i^{(n)}, \quad n = 0, 1, \cdots, \tag{2.13}$$

where the unknown $\delta \boldsymbol{U}_j^{(n)}$ is the increment, $\overline{\boldsymbol{U}}_i^{(0)}$ is the given initial guess, $\boldsymbol{R}_i^{(n)}$ is the local residual at the nth Newtonian iterative step defined by

$$\boldsymbol{R}_i^{(n)} := \sum_{e_{ij} \in \partial \mathcal{K}_i} |e_{ij}| \, \widehat{\boldsymbol{\mathcal{F}}} \left(\overline{\boldsymbol{U}}_i^{(n)}, \overline{\boldsymbol{U}}_j^{(n)}, z_i, z_j \right), \tag{2.14}$$

and the partial derivatives

$$\left(\frac{\partial \widehat{\boldsymbol{\mathcal{F}}}}{\partial \overline{\boldsymbol{U}}_i} \right)_{ij}^{(n)} := \frac{\partial \widehat{\boldsymbol{\mathcal{F}}}}{\partial \overline{\boldsymbol{U}}_i} \left(\overline{\boldsymbol{U}}_i^{(n)}, \overline{\boldsymbol{U}}_j^{(n)}, z_i, z_j \right), \tag{2.15}$$

$$\left(\frac{\partial \widehat{\boldsymbol{\mathcal{F}}}}{\partial \overline{\boldsymbol{U}}_j} \right)_{ij}^{(n)} := \frac{\partial \widehat{\boldsymbol{\mathcal{F}}}}{\partial \overline{\boldsymbol{U}}_j} \left(\overline{\boldsymbol{U}}_i^{(n)}, \overline{\boldsymbol{U}}_j^{(n)}, z_i, z_j \right), \tag{2.16}$$

contributing to the Jacobian matrix in the Newtonian method are approximately calculated by using the numerical differentiation as follows

$$\left(\left(\frac{\partial \widehat{\boldsymbol{\mathcal{F}}}}{\partial \overline{\boldsymbol{U}}_i} \right)_{ij}^{(n)} \right)_{s,k} \approx \frac{\widehat{\mathcal{F}}_s \left(\overline{\boldsymbol{U}}_i^{(n)} + \epsilon \boldsymbol{e}_k, \overline{\boldsymbol{U}}_j^{(n)}, z_i, z_j \right) - \widehat{\mathcal{F}}_s \left(\overline{\boldsymbol{U}}_i^{(n)}, \overline{\boldsymbol{U}}_j^{(n)}, z_i, z_j \right)}{\epsilon}, \tag{2.17}$$

which denotes the derivative of the sth component of vector $\widehat{\boldsymbol{\mathcal{F}}}$, denoted by $\widehat{\mathcal{F}}_s$, with respect to the kth component of vector $\boldsymbol{U}_i$, where $\boldsymbol{e}_k$ is the kth column vector of the identity matrix of the same size as $\left(\partial \widehat{\boldsymbol{\mathcal{F}}} / \partial \overline{\boldsymbol{U}}_i \right)_{ij}^{(n)}$. If an edge of the interior cell $\mathcal{K}_i$ is located on the boundary of Ω_p, then (2.17) should be replaced with

$$\left(\left(\frac{\partial \widehat{\boldsymbol{\mathcal{F}}}}{\partial \overline{\boldsymbol{U}}_i} \right)_{i\mathrm{g}}^{(n)} \right)_{s,k} \approx \frac{\widehat{\mathcal{F}}_s \left(\overline{\boldsymbol{U}}_i^{(n)} + \epsilon \boldsymbol{e}_k, \overline{\boldsymbol{U}}_{\mathrm{g}}(\overline{\boldsymbol{U}}_i^{(n)} + \epsilon \boldsymbol{e}_k), z_i, z_j \right) - \widehat{\mathcal{F}}_s \left(\overline{\boldsymbol{U}}_i^{(n)}, \overline{\boldsymbol{U}}_{\mathrm{g}}(\boldsymbol{U}_i^{(n)}), z_i, z_j \right)}{\epsilon},$$

where $\overline{\boldsymbol{U}}_{\mathrm{g}}$ denotes the approximate cell-average value of $\boldsymbol{U}$ in the ghost cell and is considered as a function of $\overline{\boldsymbol{U}}_i^{(n)}$ according to the boundary conditions given in Remark 2.3. Although the calculation of $\partial \widehat{\boldsymbol{\mathcal{F}}} / \partial \overline{\boldsymbol{U}}_i$ can also be obtained by using the chain rule, but it may be seriously tedious. Moreover, their analytical expressions are difficultly derived near the domain boundary.

The linear system (2.13) is generally singular and should be regularized. One way is to add an artificial time derivative term into (2.13). An alternative approach is to use the l^1–norm of the local residual to regularize (2.13) as follows

$$\alpha \left\| \boldsymbol{R}_i^{(n)} \right\|_{\ell^1} \delta \boldsymbol{U}_i^{(n)} + \sum_{e_{ij} \in \partial \mathcal{K}_i} |e_{ij}| \left(\frac{\partial \widehat{\boldsymbol{\mathcal{F}}}}{\partial \boldsymbol{U}_i} \right)_{ij}^{(n)} \delta \boldsymbol{U}_i^{(n)} + \sum_{e_{ij} \in \partial \mathcal{K}_i} |e_{ij}| \left(\frac{\partial \widehat{\boldsymbol{\mathcal{F}}}}{\partial \boldsymbol{U}_j} \right)_{ij}^{(n)} \delta \boldsymbol{U}_j^{(n)} = -\boldsymbol{R}_i^{(n)}, \tag{2.18}$$

where α is the positive regularization parameter. Such regularization technique has been used in solving steady-state Euler equations in [22]. Solving the linear system (2.18) for the unknown $\delta \boldsymbol{U}_j^{(n)}$ by the MG method will be discussed in Section 2.3. If the solution of

the linear system (2.18) is gotten, then the approximate solution of (2.4) can be updated by

$$\overline{\boldsymbol{U}}_i^{(n+1)} = \overline{\boldsymbol{U}}_i^{(n)} + \tau_i \delta \boldsymbol{U}_i^{(n)}, \tag{2.19}$$

where τ_i is a relaxation parameter on cell $\mathcal{K}_i$.

2.3 The geometric multigrid solver

This section extends the geometric multigrid method [22] to the linear system (2.18). The geometric multigrid methods described so far need a hierarchy of geometric grids or meshes $\{\mathcal{T}_l, l = 0, 1, \cdots, N_L\}$ for the spatial domain Ω_p, from the coarsest one ($l = N_L$) to the finest one ($l = 0$). On all levels but the coarsest one, the smoother will be applied and on the coarsest level, the system is usually solved exactly. Assume that the ratio of grid points on "neighboring" grids is constant throughout the grid hierarchy, and each coarser cell $\mathcal{K}_{i,l+1} \in \mathcal{T}_{l+1}$ is a union of several neighboring finer cells (two cells for 1D case and four cells in 2D case) in mesh $\mathcal{T}_l$, i.e.,

$$\mathcal{K}_{i,l+1} = \cup_{j \in I_{i,l+1}} \mathcal{K}_{j,l},$$

where $I_{i,l+1}$ is corresponding index set of those finer cells $\mathcal{K}_{j,l}$.

Under the above assumptions, the steady-state SWEs (1.2) are discretized and solved by the Newton iteration on the finest mesh $\mathcal{T}_0$, see Sections 2.1 and 2.2. The linear system (2.18) on $\mathcal{T}_0$ is reformulated in the following matrix-vector form

$$\sum_j \boldsymbol{A}_{ij,l} \delta \boldsymbol{U}_{j,l} = -\boldsymbol{R}_{i,l}, \ \ l = 0, \tag{2.20}$$

where the subscript l marks the mesh level, the superscript (n) in (2.18) has been omitted for convenience, and

$$\boldsymbol{A}_{ii,l} = \alpha \left\| \boldsymbol{R}_{i,l} \right\|_{\ell^1} + \sum_{e_{ij,l} \in \partial \mathcal{K}_{i,l}} |e_{ij,0}| \left(\frac{\partial \widehat{\boldsymbol{\mathcal{F}}}}{\partial \boldsymbol{U}_i} \right)_{ij,l},$$

$$\boldsymbol{A}_{ij,l} = \begin{cases} |e_{ij,l}| \left(\frac{\partial \widehat{\boldsymbol{\mathcal{F}}}}{\partial \boldsymbol{U}_j} \right)_{ij,l}, & e_{ij} \in \partial \mathcal{K}_{i,l}, \\ \boldsymbol{0}, & \text{otherwise}, \end{cases} \qquad i \neq j.$$

On the coarser mesh, the coarse mesh matrices $\boldsymbol{A}_{ij,l+1}$ are defined by using the Galerkin projection, and the source term $\boldsymbol{R}_{i,l+1}$ is derived by using the restriction operator $\boldsymbol{I}_l^{l+1}$ that restricts those on the fine mesh $\mathcal{T}_l$ to the coarse mesh $\mathcal{T}_{l+1}$, $l \geq 0$. In this paper, specifically, they are

$$\boldsymbol{A}_{ij,l+1} = \sum_{\imath \in I_{i,l+1}} \sum_{\jmath \in I_{j,l+1}} \boldsymbol{A}_{\imath\jmath,l}, \quad \boldsymbol{R}_{i,l+1} = \sum_{j \in I_{i,l+1}} \left(\boldsymbol{R}_{j,l} + \sum_{\imath} \boldsymbol{A}_{j\imath,l} \delta \boldsymbol{U}_{\imath,l} \right), \tag{2.21}$$

where $\delta \boldsymbol{U}_{j,l}$ is the (approximate) solution of (2.20) if $l = 0$, otherwise solves the following linear system

$$\sum_j \boldsymbol{A}_{ij,l} \delta \boldsymbol{U}_{j,l} = -\boldsymbol{R}_{i,l}, \quad l \geq 1. \tag{2.22}$$

As soon as the correction $\delta \boldsymbol{U}_{j,l+1}$ on the coarse mesh $\mathcal{T}_{l+1}$ is obtained, the correction $\delta \boldsymbol{U}_{j,l}$ on the fine mesh $\mathcal{T}_l$ will be improved as follows

$$\delta \boldsymbol{U}_{j,l} \longleftarrow \delta \boldsymbol{U}_{j,l} + \boldsymbol{I}_{l+1}^{l} \delta \boldsymbol{U}_{i,l+1}, \quad \forall j \in I_{i,l+1}, \tag{2.23}$$

where $\boldsymbol{I}_{l+1}^{l}$ denotes the prolongation or coarse-to-fine operator that prolongates or interpolates the correction to the fine mesh from the coarse mesh.

A multigrid cycle can be defined as a recursive procedure that is applied at each mesh level as it moves through the grid hierarchy. For example, multigrid methods with γ-cycle has the following compact recursive definition.

`Algorithm 0`: $\delta \boldsymbol{U}_{j,l} \longleftarrow \mathrm{MG}_l^{\gamma}(\delta \boldsymbol{U}_{j,l}, \boldsymbol{R}_{j,l})$

(1) Pre smoothing: Apply the smoother ν_1 times to Eq. (2.20) or (2.22) with the initial guess $\delta \boldsymbol{U}_{j,l}$.

(2) If $\mathcal{T}_l$ is the coarsest grid, i.e. $l = N_L$.

– solve the problem (2.22) with $l = N_L$.

else

– Restrict to the next coarser grid $\mathcal{T}_{l+1}$ by (2.21).

– Set initial increment on the next coarser grid: $\delta \boldsymbol{U}_{j,l+1} = 0$.

– If $\mathcal{T}_l$ is the finest grid, set $\gamma = 1$.

– Call the γ-cycle scheme γ times for the next coarser grid $\mathcal{T}_{l+1}$:

$$\delta \boldsymbol{U}_{j,l+1} \longleftarrow \mathrm{MG}_{l+1}^{\gamma}(\delta \boldsymbol{U}_{j,l+1}, \boldsymbol{R}_{j,l+1}).$$

(3) Correct with the prolongated update (2.23).

(4) Post smoothing: Apply the smoother ν_2 times to Eq. (2.20) or (2.22) with the initial guess $\delta \boldsymbol{U}_{j,l}$.

This paper only focus on two types of multigrid cycles, the V cycle ($\gamma = 1$) and W cycle ($\gamma = 2$). Fig. 2.1 shows their schematic description with $N_L = 3$, where symbols "$\circ$" and "$\bullet$" denote the pre- and post-smoothing, respectively, while the oblique lines between two symbols "$\circ$" (resp. "$\bullet$") correspond to the restriction $\boldsymbol{I}_l^{l+1}$ (resp. prolongation $\boldsymbol{I}_{l+1}^{l}$) steps. The smoother is taken as the block symmetric Gauss-Seidel (SGS) iteration.

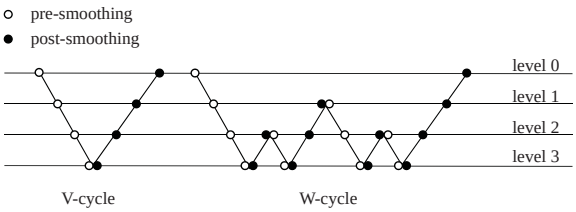

Fig. 2.1. Schematic description of a V (left) and W cycle (right) Multigrid.

2.4 Solution procedure

This section summarizes the solution procedure of our Newton multigrid method for the steady-state SWEs (1.2). It is well known that the convergence of Newtons iteration is seriously dependent on the choice of the initial guess. To overcome this difficulty, the initial guess is obtained by using the improved block lower-upper SGS (BLU-SGS) method [19] to solve (2.22) from the coarsest mesh $\mathcal{T}_{N_L}$ to the mesh $\mathcal{T}_1$ successively. The idea of BLU-SGS method is to retain the block diagonal matrices but employ LU-SGS-like backward and forward Gauss-Seidel iterations to include the implicit contributions from the off diagonal blocks. This method may be regarded as a "nonlinear extension" of the block SGS method for solving the nonlinear algebraic system (2.4).

The detailed solution procedure is illustrated by the following flowchart.

`Algorithm 1`: Newton multigrid method (abbr. `NMGM`)

Step 1: Initialization Give the "initial data" $\boldsymbol{U}(\boldsymbol{x})$ and successively refined partitions $\{\mathcal{T}_l : l = N_L, \cdots, 1, 0\}$ of the spatial domain Ω_p.

(1) Compute $\overline{\boldsymbol{U}}_{i,N_L}$, the cell average value of $\boldsymbol{U}(\boldsymbol{x})$ over the coarsest cell $\mathcal{K}_{i,N_L}$.

(2) For $l = N_L, \cdots, 1$, do the following:

- Perform the BLU-SGS iteration on the mesh $\mathcal{T}_l$ by

$$\overline{\boldsymbol{U}}_{i,l} \longleftarrow \overline{\boldsymbol{U}}_{i,l} - \left(\alpha \left\|\boldsymbol{R}_{i,l}\right\|_{\ell^1} \boldsymbol{I} + \frac{\partial \boldsymbol{R}_{i,l}}{\partial \overline{\boldsymbol{U}}_{i,l}}\right)^{-1} \boldsymbol{R}_{i,l},$$

  until $\sum\limits_i \left\|\boldsymbol{R}_{i,l}\right\|_{\ell^1} < \varepsilon_p 2^{-l}$, where $\boldsymbol{I}$ denotes the identity matrix.

- Prolongate the solution to the fine mesh from the coarse mesh by $\overline{\boldsymbol{U}}_{j,l-1} = \overline{\boldsymbol{U}}_{i,l}$ for all $j \in I_{i,l}$.

(3) Set $n = 0$ and the initial guess for Newton's iteration by $\boldsymbol{U}_{j,0}^{(0)} = \overline{\boldsymbol{U}}_{i,0}$, for all $j \in I_{i,1}$.

Step 2: Newton multigrid iteration For $n = 1, 2, \cdots, N_{\text{step}}$, do the followings.

(1) Pre smoothing: perform the BLU-SGS iteration on the finest mesh $\mathcal{T}_0$ by

$$\boldsymbol{U}_{i,0}^{(n)} \longleftarrow \boldsymbol{U}_{i,0}^{(n)} - \left(\alpha \left\|\boldsymbol{R}_{i,0}^{(n)}\right\|_{\ell^1} \boldsymbol{I} + \frac{\partial \boldsymbol{R}_{i,0}^{(n)}}{\partial \overline{\boldsymbol{U}}_{i,0}^{(n)}}\right)^{-1} \boldsymbol{R}_{i,0}^{(n)}.$$

(2) Solve (2.20) by calling `Algorithm 0` N_{mg} times.

(3) Update the solution $\boldsymbol{U}_{i,0}^{(n+1)} = \boldsymbol{U}_{i,0}^{(n)} + \tau_i \delta \boldsymbol{U}_{i,0}^{(n)}$.

Step 3: Check $\sum_i \left\| \boldsymbol{R}_{i,0}^{(n)} \right\|_{l^1} < \varepsilon$. If yes, output the results and stop; otherwise set $n \leftarrow n+1$ and go to **Step 2**.

Before ending this section, several remarks are given below.

Remark 2.4 *The parameter ϵ_p in* **Step 1** *of* `Algorithm 1` *should be chosen appropriately. If ϵ_p is very small, the cost of* **Step 1** *becomes huge so that the steady-state SWEs solver is inefficient. According to the numerical experiences,* `Algorithm 1` *works satisfactory if ϵ_p is chosen about one percent of the residual given by the initial data.*

Remark 2.5 *If the approximate solution $\boldsymbol{U}_{i,0}^{(n)}$ given in the Newton multigrid iteration satisfies $h_{i,0}^{(n)} < h_\epsilon$, the cell $\mathcal{K}_{i,0}$ is temporarily regarded as a dry cell, and the value of $\boldsymbol{U}_{i,0}^{(n)}$ is reset as zero. In our computations, $h_\epsilon = 10^{-6}$.*

Remark 2.6 *The Newton multigrid scheme in* `Algorithm 1` *can also be extended to solving the nonlinear system arising from an implicit or semi-implicit scheme for the time-dependent SWEs (1.1), e.g.*

$$\frac{\overline{\boldsymbol{U}}_i^{n+1} - \overline{\boldsymbol{U}}_i^{n}}{\Delta t_n} + \sum_{e_{ij} \in \partial \mathcal{K}_i} |e_{ij}| \left[\beta \widehat{\boldsymbol{\mathcal{F}}} \left(\overline{\boldsymbol{U}}_i^{n}, \overline{\boldsymbol{U}}_j^{n}, z_i, z_j \right) + (1-\beta) \widehat{\boldsymbol{\mathcal{F}}} \left(\overline{\boldsymbol{U}}_i^{n+1}, \overline{\boldsymbol{U}}_j^{n+1}, z_i, z_j \right) \right] = 0,$$

where Δt_n denotes the time step size, and the weight $\beta \in [0, 1)$.

3 Numerical Experiments

The section presents several numerical examples to demonstrate the robustness and efficiency of `NMGM` for 1D and 2D steady-state SWEs (1.2), and investigates the relation between the convergence behavior of `NMGM` and the distribution of the eigenvalues of the iteration matrix detailedly. Unless specifically stated, the parameter ϵ_p in the initialization step of `Algorithm 1` is taken as 0.2, and the multigrid iteration number N_{mg} is set to be 2 (resp. 3) for 1D (resp. 2D) problems. Moreover, the parameters ϵ in (2.17), α in (2.18), and τ_i in (2.19) are always taken as 10^{-8}, 3, and 1, respectively. All computations are carried out on the Linux environment of a personal computer of Lenovo (Intel(R) Core(TM) i5 CPU 3.2GHZ 4GB RAM).

3.1 1D case

Example 3.1 (Smooth subcritical flow) This problem has been studied in [7] to check the dissipative and dispersive errors in the kinetic schemes. The bottom shape of the river

is

$$z(x) = 0.2\mathrm{e}^{-\frac{(x+1)^2}{2}} + 0.3\mathrm{e}^{-(x-1.5)^2}, \quad x \in [-10, 10],$$

and the boundary conditions at $x = \pm 10$ are specified as $h = 1$ and $hu = 1$. Fig. 3.1 shows the numerical steady-state solutions obtained by NMGM on the mesh of 512 uniform cells, in comparison with the exact solutions obtained by solving the algebraic system

$$u^3 + (2gz - 2g - 1)u + 2g = 0, \quad hu = 1.$$

Fig. 3.2 displays the numerical residuals obtained by NMGM versus the NMGM iteration number N_{step} and CPU time for three meshes of 512, 1024, and 2048 uniform cells respectively. The results show that NMGM is very efficient and fast to get the correct steady-state solutions. Moreover, the convergence behaviors are similar on those different meshes, and the NMGM iteration number does not increase with refining the mesh. In those computations, the HLL flux is used, and the grid level number in the V-cycle multigrid is set to be 4, i.e. $N_L = 3$.

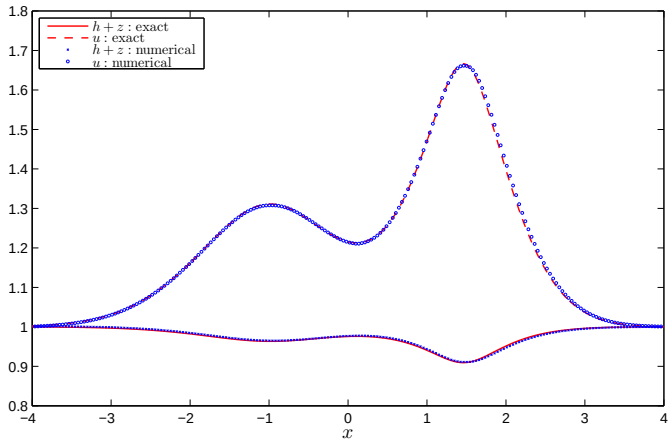

Fig. 3.1. Example 3.1: Close-up of the steady-state solutions $h + z$ and u obtained by NMGM on the mesh of 512 uniform cells.

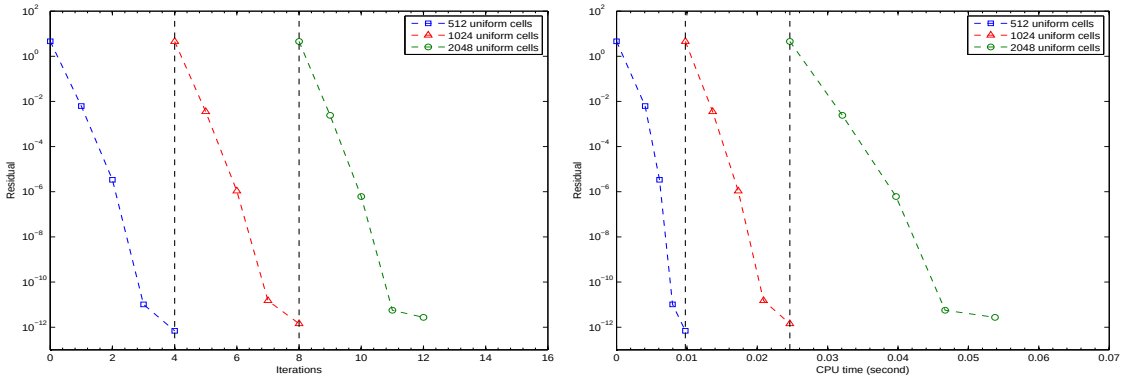

Fig. 3.2. Example 3.1: Residuals vs NMGM iteration number (left) and CPU time (right) for three uniform meshes.

Table 3.1 investigates the effect of the HLL, LLF, and Roe fluxes shown in Remark 2.2 on the convergence behavior of NMGM, in comparison to the BLU-SGS iteration in solving (2.18), where N, N_L, N_{step}, and T_{cpu} denote the cell number, the coarse mesh

Table 3.1
Example 3.1: Effect of the HLL, LLF, and Roe fluxes on convergence behaviors of NMGM and the BLU-SGS iteration.

N			64	128	256	512	1024	2048
HLL	Block	N_{step}	33	39	40	47	49	58
	LU-SGS	T_{cpu}	6.57e-3	1.25e-2	1.68e-2	3.29e-2	4.87e-2	1.0e-1
	V-cycle	N_{step}	4	4	3	4	4	4
	$N_L = 1$	T_{cpu}	2.51e-3	4.81e-3	5.37e-3	9.01e-3	1.37e-2	2.63e-2
	V-cycle	N_{step}	4	4	3	4	4	4
	$N_L = 3$	T_{cpu}	2.75e-3	4.83-3	6.04e-3	9.78e-3	1.49e-2	2.91e-2
	ρ		0.39347	0.43938	0.46526	0.47874	0.48541	0.48877
	R_∞		0.93276	0.82239	0.76517	0.73660	0.72276	0.71586
LLF	Block	N_{step}	576	1370	3156	7116	15437	31855
	LU-SGS	T_{cpu}	4.18e-2	1.65e-1	5.44e-1	2.66e0	1.08e1	4.22e1
	V-cycle	N_{step}	22	51	118	269	585	1224
	$N_L = 1$	T_{cpu}	6.21e-3	2.65e-2	8.56e-2	3.67e-1	1.55e0	6.33e0
	V-cycle	N_{step}	8	9	23	55	125	267
	$N_L = 3$	T_{cpu}	4.93e-3	9.67e-3	1.90e-2	8.45e-2	3.69e-1	1.54e0
	V-cycle	N_{step}	7	8	8	12	26	64
	$N_L = 5$	T_{cpu}	2.17e-3	6.23e-3	1.04e-2	1.91e-2	7.93e-2	3.63e-1
	W-cycle	N_{step}	6	6	7	7	8	8
	$N_L = 5$	T_{cpu}	6.67e-3	9.87e-3	1.39e-2	2.38e-2	4.94e-2	9.95e-2
	ρ		0.96013	0.98273	0.99256	0.99673	0.99851	0.99929
	R_∞		4.069e-2	1.742e-2	7.468e-3	3.274e-3	1.493e-3	7.072e-4
ROE	Block	N_{step}	35	38	39	43	45	51
	LU-SGS	T_{cpu}	6.07e-3	9.85e-3	2.18e-2	3.74e-2	5.58e-2	1.19e-1
	V-cycle	N_{step}	4	5	5	5	5	5
	$N_L = 1$	T_{cpu}	3.06e-3	7.68e-3	9.57e-2	1.31e-2	2.06e-2	4.12e-2
	V-cycle	N_{step}	4	5	5	5	5	5
	$N_L = 3$	T_{cpu}	3.23e-3	7.79e-3	1.05e-1	1.42e-2	2.20e-2	4.29e-2
	ρ		0.48516	0.49799	0.50571	0.50827	0.50655	0.49969
	R_∞		0.72327	0.69717	0.68178	0.67673	0.68012	0.69377

level number of the geometric MG, the total Newton iteration number, and the CPU time T_{cpu}, respectively, ρ denotes the spectral radius of the iteration matrix of the block SGS method around the steady-state solution, and $R_\infty := -\ln \rho$ corresponds to the asymptotic convergence rate. The results show that NMGM is a little more efficient than the BLU-SGS iteration for the HLL and Roe fluxes, and exhibits great advantages for the LLF flux, specially, in the case of the W-cycle multigrid with $N_L = 5$. The W-cycle multigrid is also tested for the HLL and Roe fluxes, and its performance is almost the same as the V-cycle multigrid. The BLU-SGS iteration with the HLL and Roe fluxes are more efficient than the LLF flux. For the former, N_{step} increases very slowly with refining the mesh, but the latter does nearly linearly increase in terms of the cell number N. Such phenomenon could be explained by comparing the spectral radius ρ of the iteration matrix, whose values are around 0.5 and larger than 0.9, respectively. Fig. 3.3(a) displays the distribution (in the complex plane) of the eigenvalues of the block SGS iteration matrix on the mesh with 256

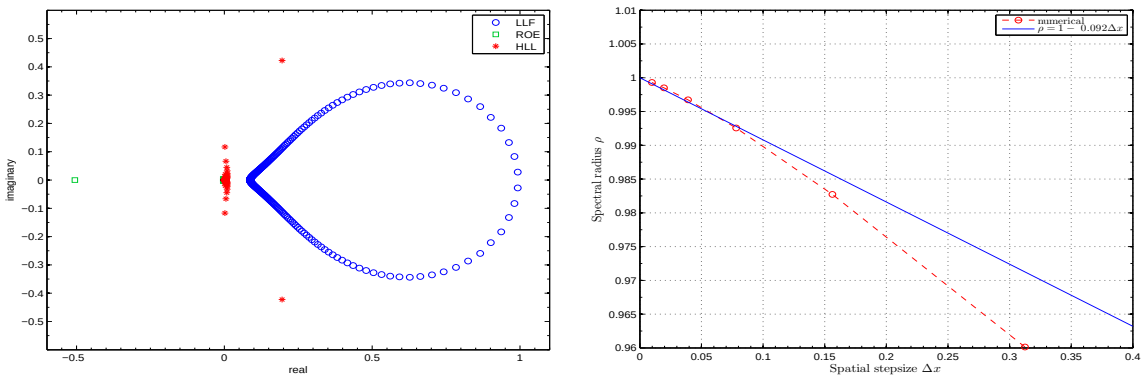

(a) (b)

Fig. 3.3. Example 3.1: (a). Distribution of the eigenvalues of the block SGS iteration matrix for three numerical fluxes over the mesh of 256 uniform cells. (b). Asymptotic relation of the spectral radius ρ of the block SGS iteration matrix with respect to the spatial step size Δx for the LLF flux.

uniform cells for the HLL, LLF, and Roe fluxes. We see that the eigenvalues are almost around 0 for the HLL flux (except for two eigenvalues with relatively large imaginary parts of ± 0.4 respectively) and the Roe flux (except for only one eigenvalue located around -0.5), while those are widely distributed for the LLF flux (some of them are near 1). Thus the "high frequency" eigenvalues for the LLF flux are much more than for the HLL and Roe fluxes. Fig. 3.3(b) plots an asymptotic relation of the spectral radius ρ of the iteration matrix with respect to the spatial step size Δx for the LLF flux as follows

$$\rho \sim 1 - C\Delta x, \quad \text{as } \Delta x \to 0, \tag{3.1}$$

where C is about 0.092.

Example 3.2 (Two transcritical flows over a bump) The example simulates two transcritical flows over a bump, which have been widely used to test the SWEs solvers [3,7,29]. The bed topography is

$$z(x) = \begin{cases} 0.2 - 0.05(x-10)^2, & 8 < x < 12, \\ 0, & \text{otherwise}, \end{cases} \tag{3.2}$$

for a channel of length 25.

(I). Transcritical flow without a shock: The discharge $hu = 1.53$ is imposed at the upstream boundary condition $x = 0$ while the water height $h = 0.66$ is imposed at the downstream end of the channel $x = 25$ when the flow is sub-critical.

Fig. 3.4 shows the numerical steady-state solution $h + z$ obtained by using the HLL flux and the V-cycle multigrid with $N_L = 3$ on the mesh of 512 uniform cells in comparison to the exact solution given by `SWASHES` [30]. Fig. 3.5 gives the convergence history of `NMGM` in terms of the `NMGM` iteration number N_{step} and CPU time on three meshes of 512, 1024, and 2048 uniform cells respectively. The results show that the steady-state solutions can

be correctly and fast obtained by using NMGM, the convergence behaviors are similar to Example 3.1, and the NMGM iteration number does not increase with the mesh refinement.

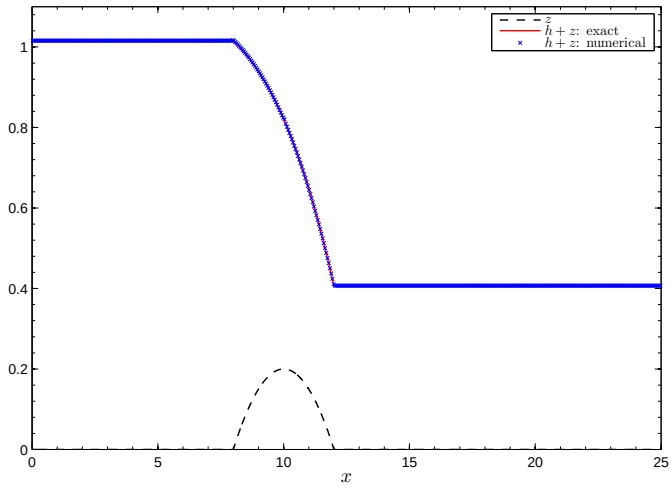

Fig. 3.4. Example 3.2(I): Steady-state solution $h + z$ obtained by NMGM on the mesh of 512 uniform cells.

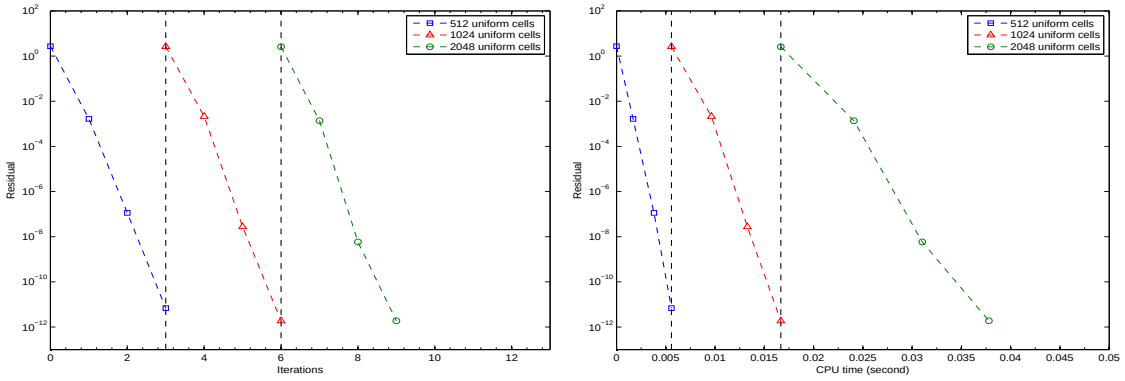

Fig. 3.5. Example 3.2(I): Convergence history in terms of the NMGM iteration number N_{step} (left) and CPU time (right) on three uniform meshes.

Similar to Table 3.1, Table 3.2 investigates the effect of the HLL, LLF, and Roe fluxes on the convergence behavior of NMGM, in comparison to the BLU-SGS iteration. The convergence behaviors of NMGM and the BLU-SGS iteration are almost the same as those in Example 3.1. The distribution (in the complex plane) of the eigenvalues of the block SGS iteration matrix in Fig. 3.6(a) shows that the "high frequency" eigenvalues for the LLF flux are much more than for HLL or Roe flux, Fig. 3.6(b) shows that the spectral radius ρ of the iteration matrix has asymptotic relation (3.1) with $C \sim 0.3$ for the LLF flux in terms of the spatial step size Δx.

(II). Transcritical flow with a shock: The discharge hu is taken as 0.18 on the upstream boundary, and $h = 0.33$ is specified on the downstream boundary condition. In this case, the Froude number $F_r = u/\sqrt{gh}$ increases to a value larger than 1 above the bump, and then decreases to less than 1.

Fig. 3.7 shows the numerical steady-state solution on the mesh of 512 uniform cells in

Table 3.2
Example 3.2(I): Effect of the HLL, LLF, and Roe fluxes on convergence behaviors of NMGM and the BLU-SGS iteration.

N			64	128	256	512	1024	2048
HLL	Block	N_{step}	25	28	31	31	32	33
	LU-SGS	T_{cpu}	8.87e-3	1.11e-2	1.43e-2	1.76e-2	2.85e-2	5.21e-2
	V-cycle	N_{step}	3	3	3	3	3	3
	$N_L = 1$	T_{cpu}	1.88e-3	2.24e-3	4.52e-3	8.54e-3	1.24e-2	2.07e-2
	V-cycle	N_{step}	3	3	3	3	3	3
	$N_L = 3$	T_{cpu}	1.96e-3	3.31e-3	6.44e-3	9.16e-2	1.30e-2	2.09e-2
	ρ		0.36309	0.38504	0.41148	0.47183	0.4518	0.46042
	R_∞		1.0131	0.9544	0.8879	0.7511	0.7945	0.7756
LLF	Block	N_{step}	373	481	878	1667	3277	6462
	LU-SGS	T_{cpu}	3.67e-2	5.65e-2	1.74e-1	6.17e-1	2.31e0	8.73e0
	V-cycle	N_{step}	13	20	35	66	128	249
	$N_L = 1$	T_{cpu}	7.89e-3	1.14e-2	2.48e-1	9.09e-1	3.40e-1	1.27e0
	V-cycle	N_{step}	14	16	17	18	31	59
	$N_L = 3$	T_{cpu}	9.42e-3	1.02e-2	1.35e-2	2.78e-2	9.12e-2	3.43e-1
	V-cycle	N_{step}	14	17	18	19	20	22
	$N_L = 5$	T_{cpu}	9.67e-3	1.15e-2	1.51e-2	3.02e-2	6.11e-2	1.31e-1
	W-cycle	N_{step}	11	12	9	8	8	8
	$N_L = 5$	T_{cpu}	6.73e-3	1.06e-2	1.48e-2	2.50e-2	4.95e-2	9.63e-2
	ρ		0.92458	0.94598	0.97116	0.98515	0.99246	0.9962
	R_∞		7.842e-2	5.553e-2	2.936e-2	1.496e-2	7.566e-3	3.805e-3
ROE	Block	N_{step}	15	21	31	49	88	172
	LU-SGS	T_{cpu}	4.42e-3	1.06e-2	1.68e-2	3.82e-2	1.08e-1	4.10e-1
	V-cycle	N_{step}	3	3	3	3	4	5
	$N_L = 1$	T_{cpu}	2.68e-3	5.01e-3	8.33e-3	1.16e-2	1.82e-2	4.52e-2
	V-cycle	N_{step}	3	3	3	3	4	4
	$N_L = 3$	T_{cpu}	2.70e-3	5.10e-3	8.54e-3	1.36e-2	1.85e-2	3.63e-2
	ρ		0.16498	0.33576	0.53079	0.70641	0.83135	0.90858
	R_∞		1.802e0	1.091e0	6.334e-1	3.476e-1	1.847e-1	9.587e-2

comparison to the exact solution [30] where a stationary shock appears and is well resolved. Fig. 3.8 gives the convergence history of NMGM versus the NMGM iteration number N_{step} and CPU time on three meshes of 512, 1024, and 2048 uniform cells respectively. The results show that NMGM is very efficient and fast to get the correct steady-state solution with a shock, the convergence behaviors are almost similar on three uniform meshes, and the iteration number N_{step} scarcely changes with the mesh refinement. The HLL flux and V-cycle multigrid with $N_L = 3$ have been adopted in those computations.

The effect of the HLL, LLF, and Roe fluxes on the convergence behavior of NMGM and the BLU-SGS iteration. is investigated in Table 3.3, which shows that the NMGM performs much more efficiently than the BLU-SGS iteration, and it becomes obvious as N_L increases in the multigrid and the W-cycle multigrid is adopted with the LLF flux. Moreover, convergence behaviors depend on the numerical flux, and the block LU-SGS method with the HLL

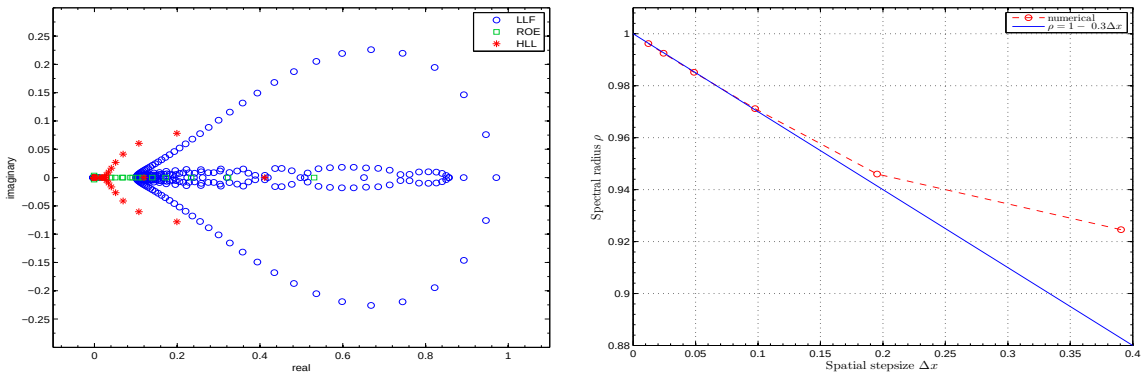

(a) (b)

Fig. 3.6. Example 3.2(I): (a). Distribution of the eigenvalues of the block SGS iteration matrix with the HLL, LLF, Roe fluxes over the mesh of 256 uniform cells. (b). Asymptotic relation of the spectral radius ρ of the block SGS iteration matrix with respect to the spatial stepsize Δx for LLF flux.

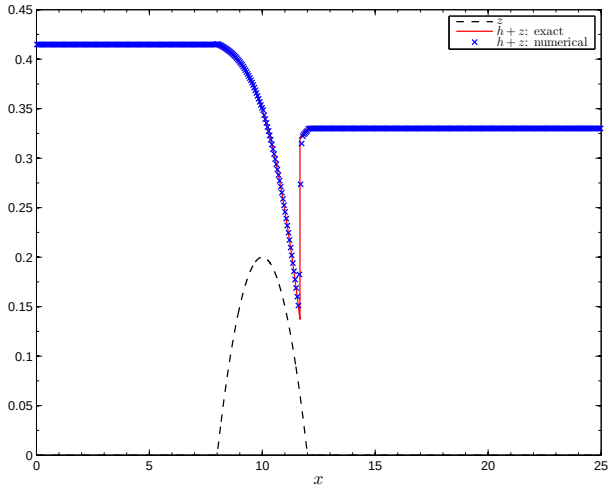

Fig. 3.7. Example 3.2(II): Steady-state solution $h + z$ obtained by NMGM on the mesh of 512 uniform cells.

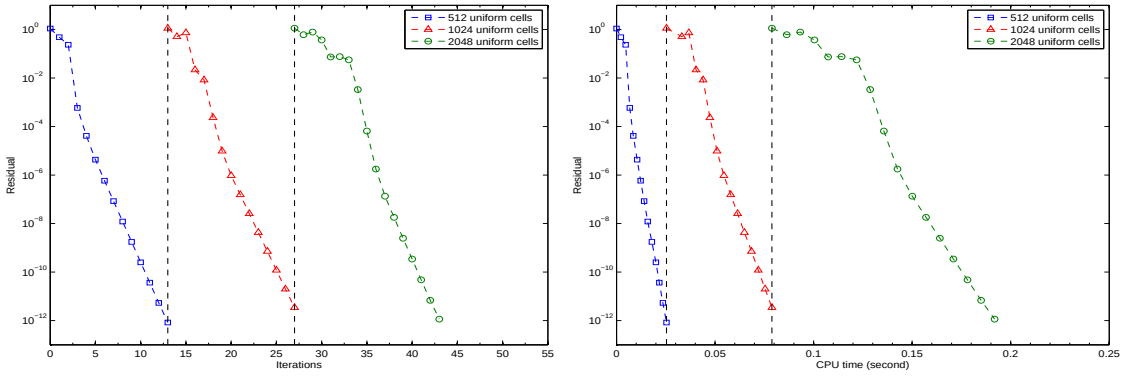

Fig. 3.8. Example 3.2(II): Convergence history in terms of the NMGM iteration number N_{step} (left) and CPU time (right) on three uniform meshes.

Table 3.3
Example 3.2(II): Effect of the HLL, LLF, and Roe fluxes on convergence behaviors of NMGM and the BLU-SGS iteration.

N			64	128	256	512	1024	2048
HLL	Block	N_{step}	28	37	82	161	328	658
	LU-SGS	T_{cpu}	2.87e-3	7.07e-3	2.94e-2	1.07e-1	4.88e-1	1.92e0
	V-cycle	N_{step}	4	4	4	13	14	28
	$N_L = 1$	T_{cpu}	2.62e-3	4.49e-3	7.99e-3	2.52e-2	4.68e-2	1.73e-1
	V-cycle	N_{step}	4	4	5	13	14	16
	$N_L = 3$	T_{cpu}	2.87e-3	5.27e-3	8.64e-3	2.54e-2	5.35e-2	1.13e-1
	V-cycle	N_{step}	4	4	5	13	14	16
	$N_L = 5$	T_{cpu}	2.96e-3	5.32e-3	8.89e-3	3.76e-2	5.44e-2	1.14e-1
	ρ		0.39173	0.52614	0.74702	0.86591	0.93346	0.96696
	R_∞		9.372e-1	6.422e-1	2.917e-1	1.44e-1	6.885e-2	3.36e-2
LLF	Block	N_{step}	288	662	1424	3084	6518	13179
	LU-SGS	T_{cpu}	1.64e-2	9.59e-2	2.61e-1	1.91e0	6.01e0	2.60e1
	V-cycle	N_{step}	12	25	52	113	242	488
	$N_L = 1$	T_{cpu}	6.29e-3	2.37e-2	4.93e-2	1.55e-1	6.43e-1	2.49e0
	V-cycle	N_{step}	8	8	14	28	53	103
	$N_L = 3$	T_{cpu}	4.98e-3	9.84e-3	1.51e-2	4.73e-2	1.56e-1	5.99e-1
	V-cycle	N_{step}	8	9	10	10	17	47
	$N_L = 5$	T_{cpu}	5.13e-3	1.16e-2	1.71e-2	2.28e-2	5.27e-2	2.76e-1
	W-cycle	N_{step}	7	6	6	7	7	10
	$N_L = 5$	T_{cpu}	7.62e-3	1.27e-2	1.73e-2	2.23e-2	4.49e-2	1.24e-1
	ρ		0.92518	0.96734	0.98529	0.99604	0.99663	0.99834
	R_∞		7.777e-2	3.321e-2	1.482e-2	6.987e-3	3.378e-3	1.659e-3
ROE	Block	N_{step}	19	26	36	102	204	378
	LU-SGS	T_{cpu}	1.52e-3	4.13e-3	1.32e-2	6.37e-2	2.45e-1	9.04e-1
	V-cycle	N_{step}	3	4	4	12	10	18
	$N_L = 1$	T_{cpu}	2.26e-3	5.83e-3	1.09e-2	2.98e-2	3.88e-2	1.34e-1
	V-cycle	N_{step}	3	4	4	12	11	12
	$N_L = 3$	T_{cpu}	2.42e-3	6.37e-3	1.22e-2	3.05e-2	4.59e-2	9.86e-2
	V-cycle	N_{step}	3	4	4	12	11	12
	$N_L = 5$	T_{cpu}	2.61e-3	6.64e-3	1.26e-2	3.10e-2	4.79e-2	1.01e-1
	ρ		0.25371	0.36652	0.54545	0.79807	0.89694	0.9425
	R_∞		1.372e0	1.004e0	6.062e-1	2.256e-1	1.088e-1	5.922e-2

or Roe flux is more efficient than the LLF flux. Such observation is consistent with the previous. However, different from the results of Example 3.1 and 3.2(I), the results in Table 3.3 show that N_{step} increases almost linearly with the mesh refinement for the BLU-SGS iteration with the HLL, LLF, and Roe fluxes, and the spectral radius ρ of the iteration matrix increases asymptotically to 1 as N increases. The distribution in the complex plane of the eigenvalues of the block SGS iteration matrix in Fig. 3.9(a) still shows that the "high frequency" eigenvalues for the LLF flux are much more than for the HLL or Roe flux. Figs. 3.9(b-d) show the asymptotic relation (3.1) of ρ with respect to the spatial step size Δx, where C is about $2.58, 0.15$, and 4.53 for the HLL, LLF, and Roe fluxes,

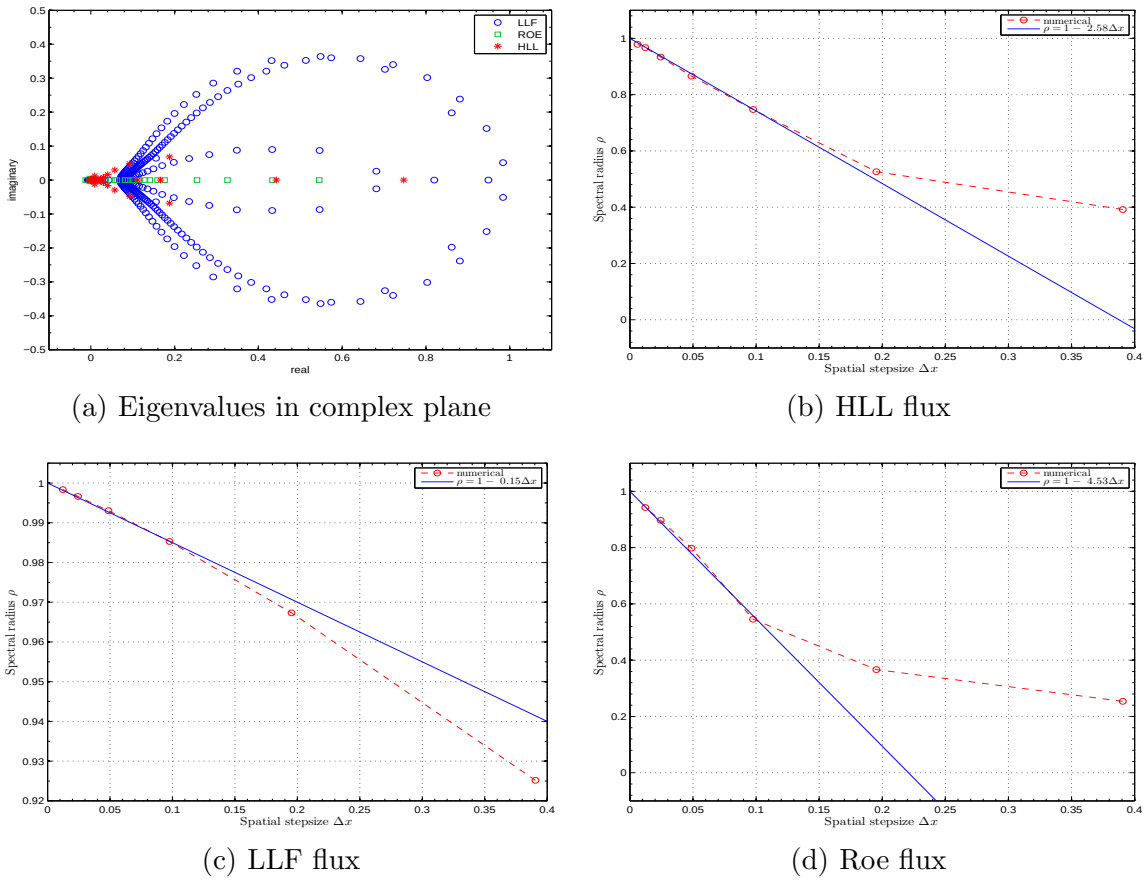

(a) Eigenvalues in complex plane

(b) HLL flux

(c) LLF flux

(d) Roe flux

Fig. 3.9. Example 3.2(II): (a). Distribution of the eigenvalues of the block SGS iteration matrix with the HLL, LLF, and Roe fluxes on the mesh of 256 uniform cells. (b-d). Asymptotic relation of the spectral radius ρ of the block SGS iteration matrix with respect to the spatial step size Δx.

respectively.

Example 3.3 (Wet-dry boundary problem) The bed topography for this problem is the same as one in Example 3.2, but for a channel of length 20. Initially, the flow with the water height $h^{(0)}(x) = 0.22 - z(x)$ is static in the channel, i.e., $u(x) = 0$. A steady state with the dry bed

$$\begin{cases} h(x) = \max\{0.1 - z(x), 0\}, \\ u(x) = 0, \end{cases}$$

will be reached if imposing $h = 0.1$ at the interval ends $x = 0$ and 20. Since the steady solution involves wet/dry transition, the Jacobian matrix of these numerical fluxes near the wet-dry boundary becomes singular so that it is much more difficult and challenging.

Fig. 3.10 shows the steady solutions $h + z$ and the error in the rest water surface obtained on the mesh of 512 uniform cells, where the LLF flux and W-cycle multigrid with $N_L = 3$ are used. It is seen that the correct steady solutions are efficiently obtained by `NMGM`, and the rest water surface is preserved exactly up to the machine precision. Fig. 3.11 gives

the convergence history of NMGM in terms of the NMGM iteration number N_{step} and CPU time on four meshes of 512, 1024, 2048, and 4096 uniform cells, respectively. Convergence behaviors of NMGM and N_{step} do not depend on the uniform mesh number N.

Because NMGM and the BLU-SGS iteration with the HLL or Roe flux fail to work now, Table 3.4 only investigates the convergence behaviors of NMGM and the BLU-SGS iteration with the LLF flux. We see that NMGM is much more efficient than the BLU-SGS iteration and it is obvious as N_L increases and the W-cycle multigrid is adopted. In this problem, the big solution error is mainly introduced around the wet-dry boundary and can be fast reduced by using the W-cycle multigrid with properly increasing the coarse level number N_L.

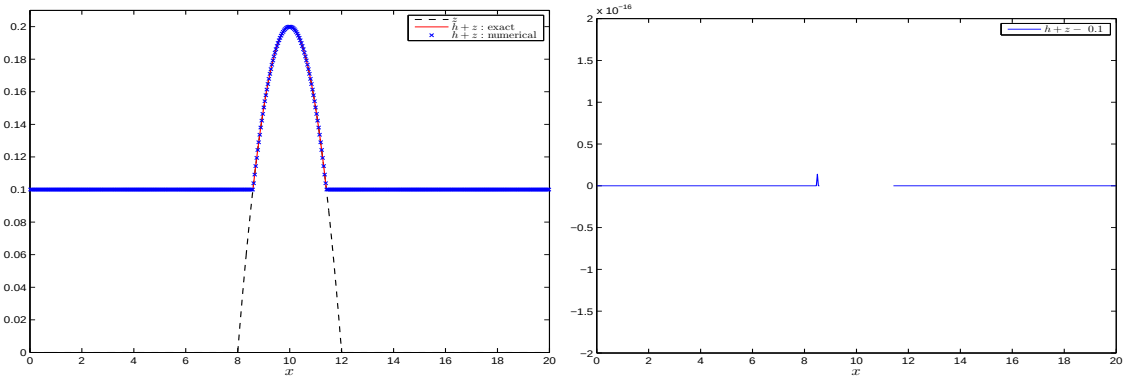

Fig. 3.10. Example 3.3: Steady-state solution (left) and the error in the water surface (right) obtained by NMGM on the mesh of 512 uniform cells.

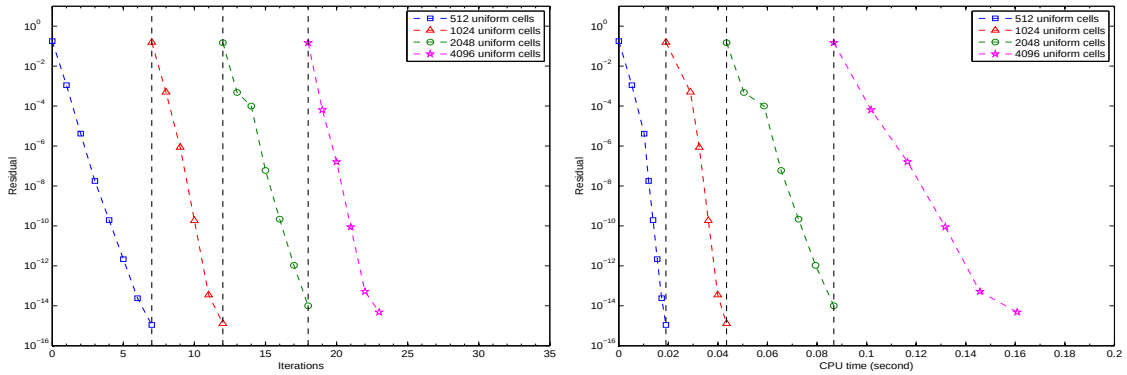

Fig. 3.11. Example 3.3: Convergence history in terms of the NMGM iteration number N_{step} (left) and CPU time (right) on four uniform meshes.

3.2 2D case

Unless specifically stated, in the following, the HLLC flux and V-cycle multigrid are adopted, and the coarse mesh level number N_L is set to be 3.

Example 3.4 The first 2D example is to simulate fluid flows in two symmetric channels with flat bottom constricted from both side in the y–direction, see [8]. Specifically, *channel*

Table 3.4
Example 3.3: Convergence behaviors of NMGM and the BLU-SGS iteration with different N_L, V or W cycle multigrid, and LLF flux.

N		64	128	256	512	1024	2048	4096
Block	N_{step}	42	69	129	364	1122	4009	14459
LU-SGS	T_{cpu}	8.16e-3	1.78e-2	3.41e-2	1.37e-1	7.71e-1	5.17e0	3.63e1
V-cycle	N_{step}	4	5	6	11	32	110	356
$N_L = 1$	T_{cpu}	1.73e-3	4.12e-3	1.03e-2	2.30e-2	8.13e-2	4.91e-1	3.08e0
V-cycle	N_{step}	4	5	5	7	9	11	44
$N_L = 3$	T_{cpu}	2.02e-3	4.58e-3	9.82e-3	1.63e-2	2.55e-2	5.92e-2	4.23e-1
V-cycle	N_{step}	4	5	5	7	9	12	12
$N_L = 5$	T_{cpu}	2.07e-3	4.76e-3	1.01e-2	1.76e-2	2.64e-2	6.06e-2	1.18e-1
W-cycle	N_{step}	4	5	6	8	18	58	198
$N_L = 1$	T_{cpu}	1.91e-3	4.62e-3	1.16e-2	1.72e-2	4.82e-2	2.85e-1	1.94e0
W-cycle	N_{step}	4	5	5	7	5	6	5
$N_L = 3$	T_{cpu}	2.58e-3	5.78e-3	1.90e-2	2.45e-2	2.93e-2	4.33e-2	7.40e-2
ρ		0.45675	0.63258	0.80392	0.92105	0.97479	0.99296	0.99816
R_∞		7.836e-1	4.579e-1	2.183e-1	8.224e-2	2.553e-2	7.062e-3	1.846e-3

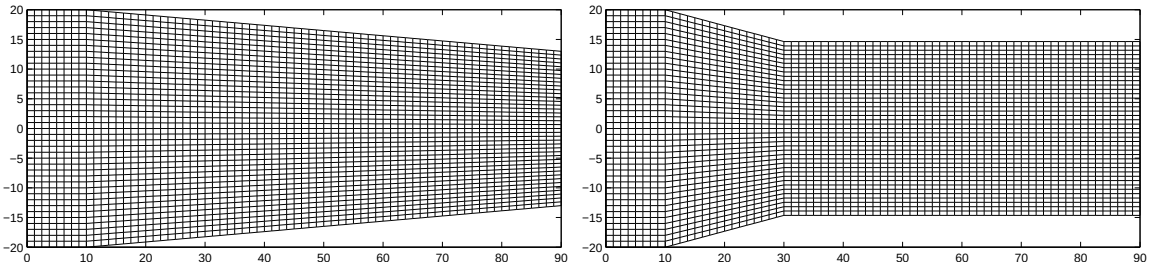

Fig. 3.12. Example 3.4: The geometries of *channel I* (left) and *II* (right) and structured mesh of 72×40 cells.

I is with a constriction angle $\alpha = 5^\circ$ started at $x = 10$, and *channel II* with a constriction angle $\alpha = 15^\circ$ started at $x = 10$, ended at $x = 30$, and then followed by a straight narrower channel, see Fig. 3.12 for their geometries and corresponding structured mesh of 72×40 cells. The inflow conditions $h = 1$ and $v = 0$ and the Froude number $F_r = |\boldsymbol{u}|/\sqrt{gh} = 2.5$ are imposed at $x = 0$, the outflow boundary condition is specified at $x = 90$, while slip boundary conditions are employed on the top and bottom boundaries.

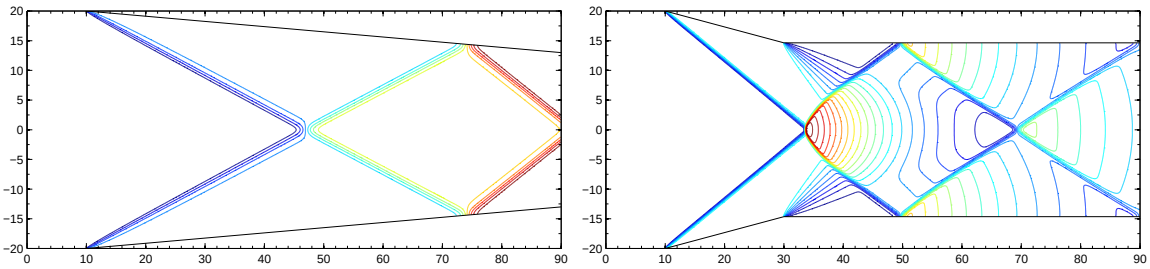

Fig. 3.13. Example 3.4: The steady water depth h with 13 and 20 equally spaced contour lines for *channel I* and *II* obtained by NMGM on the mesh of 576×320 cells, respectively.

Fig. 3.13 displays the contour plots of the steady solutions for two channels obtained by

NMGM on the mesh of 576×320 cells. For the steady state flow in *channel I*, two bore waves starting at the points $(10, \pm 20)$ interact at the point (45,0) and then two regular reflections happen around $x = 74$ due to the constriction. The present result is well comparable to the numerical result given by using the adaptive moving mesh method to solve the time-dependent SWEs [8] and analytical ones [31], especially, numerical values of the water heights of the first and second plateau are 1.25 and 1.5271, respectively, which agree well with those in [8,31]. For the steady flows in *channel II*, two shock waves started at $(10, \pm 20)$ meet around (33,0) each other, then interact with two expansion waves generated at the points $(30, \pm 15)$, and then two regular reflections happen at $(50, \pm 15)$. Finally, two reflected shock waves meet around (69,0). From the contour plots in Fig. 3.13, we see that NMGM can well capture those waves and their interactions with high resolution and non-oscillation.

Figs. 3.14 and 3.15 show the convergence history of NMGM versus the NMGM iteration number N_{step} and CPU time on three successively refined meshes for *channel I* and *channel II*, respectively. It is seen that NMGM works successfully on those meshes and the convergence behaviors of NMGM are independent on the cell number N. Compared to *channel I*, the computation of the steady solution for *channel II* seems more difficult for NMGM and takes more iteration steps. In those computations, $\epsilon_p = 2 \times 10^2$.

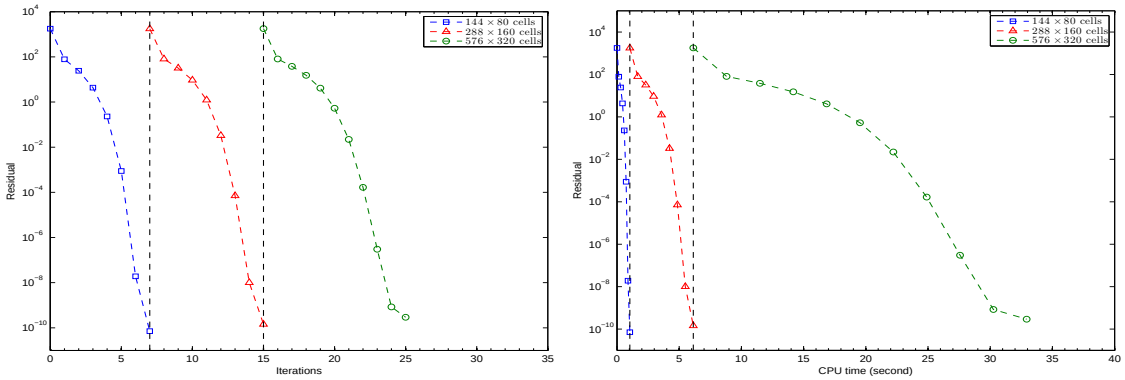

Fig. 3.14. Example 3.4: Convergence history in terms of the NMGM iteration number N_{step} (left) and CPU time (right) on three meshes for *channel I*.

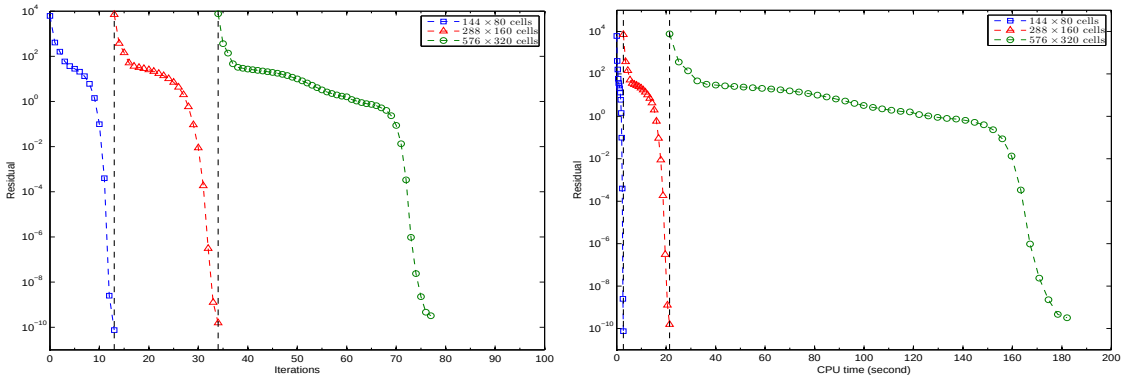

Fig. 3.15. Same as Fig.3.14, except for *channel II*.

Example 3.5 This example is to solve another channel constriction problem [32], in

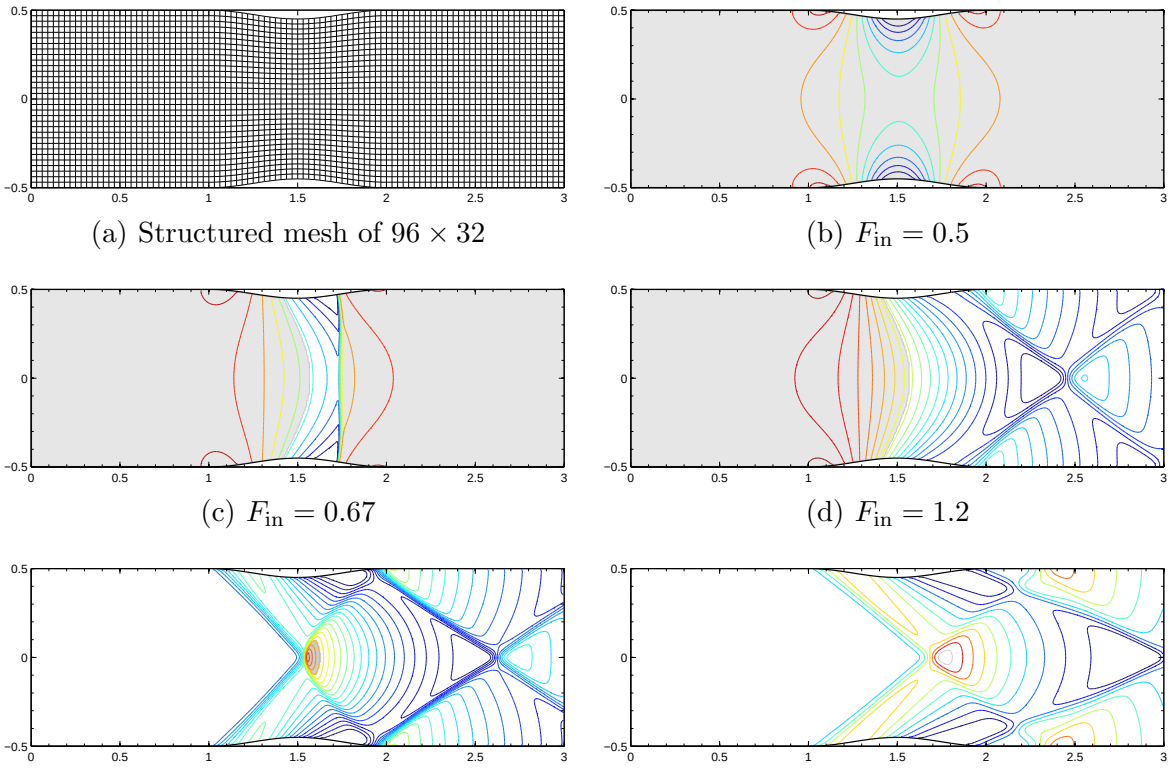

(a) Structured mesh of 96×32 (b) $F_{\text{in}} = 0.5$

(c) $F_{\text{in}} = 0.67$ (d) $F_{\text{in}} = 1.2$

(e) $F_{\text{in}} = 1.7$ (f) $F_{\text{in}} = 2$

Fig. 3.16. Example 3.5: The structured mesh of 96×32 cells and the contours of steady water depth h with the shaded subcritical regions obtained by NMGM on the mesh of 384×128 cells.

which a channel of length 3 units is with a symmetric constriction of length 1 unit at its center $x = 1.5$ and the variable width

$$W(x) = \begin{cases} 1 - (1 - W_{\min}) \cos^2(\pi(x - 1.5)), & |x - 1.5| \le 0.5, \\ 1, & \text{otherwise}, \end{cases}$$

where $W_{\min}$ is the minimum channel width, see Fig. 3.16(a) for its geometry and corresponding structured mesh of 96×32 cells. Boundary conditions are specified as follows:

$hu = h_0 F_{\text{in}} \sqrt{g h_0}$, $hv = 0$ for subcritical inflow,
$h = h_0$ for subcritical outflow,
$hu = h_0 F_{\text{in}} \sqrt{g h_0}$, $hv = 0$, $h = h_0$ for a supercritical inflow,
supercritical outflow boundary condition at $x = 3$,
slip boundary conditions on the top and bottom boundaries,

Our computations take $h_0 = 1$, $W_{\min} = 0.9$, and $F_{\text{in}} = 0.5, 0.67, 1.2, 1.7$, and 2, respectively, investigate the effect of the Froude number F_{in} on the convergence of NMGM, and demonstrate the robustness of NMGM. Figs. 3.16(b-f) display the contours of steady water depth h obtained by NMGM on the mesh of 384×128 cells, where the subcritical region (in which the Froude number $F_r(\boldsymbol{x}) < 1$) has been shaded. Those plots show that the

steady solutions resolved by NMGM are non-oscillatory and the symmetry of the flow is well preserved. Those results are very similar to those in [32], and five different types of steady flow pattern can be observed as follows.

- Case 1 ($F_{\text{in}} = 0.5$): The flow is smooth and purely subcritical.
- Case 2 ($F_{\text{in}} = 0.67$): The flow is subcritical at inflow and outflow, critical at the channel throat, and with a steady discontinuity in the divergent region of the channel.
- Case 3 ($F_{\text{in}} = 1.2$): The flow shows the cross-wave pattern with the oblique downstream jumps, and is subcritical at inflow, critical at the throat, and supercritical at outflow.
- Case 4 ($F_{\text{in}} = 1.7$): The flow is supercritical at inflow and outflow, and with oblique jumps and a subcritical pocket within the constriction.
- Case 5 ($F_{\text{in}} = 2$): The flow is purely supercritical everywhere throughout the channel.

The convergence history of NMGM in terms of the NMGM iteration number N_{step} on three meshes are presented in Figs. 3.17(a)-(e). It is seen that NMGM exhibits good robustness and works well on those meshes for the above steady flows. Case 2 requires more iteration steps than the other cases. Fig. 3.17(f) gives histogram of the NMGM iteration number N_{step} of NMGM in terms of the Froude number F_{in} on the mesh of 384×128 cells. We further see that NMGM requires more iteration steps when the Froude number F_{in} is less than 0.3 or equal to 0.7.

Example 3.6 The test describes a transcritical flow over a 2D bump, which is a 2D extension of Example 3.2. The bottom topography is defined by

$$z(x,y) = \begin{cases} 0.2 - 0.05\left((x-10)^2 + y^2\right), & (x-10)^2 + y^2 < 4, \\ 0, & \text{otherwise}, \end{cases}$$

in the channel of $[0, 25] \times [-5, 5]$. The discharge $hu = 1.53, hv = 0$ is imposed at $x = 0$, the water height $h = 0.52$ is imposed at the downstream $x = 25$, and the reflective boundaries are specified at $y = \pm 5$ in the y–direction.

The contours of the steady water surface $h + z$ obtained by NMGM are displayed in Fig. 3.18 on the mesh of 640×320 uniform cells, where the subcritical region is shaded. In the steady flow, the cross-wave pattern with the oblique downstream jumps is observed. Moreover, the flow varies from subcritical at inflow to supercritical at outflow, and is similar to the 1D Example 3.2(I). The efficiency of NMGM are demonstrated in Fig. 3.19 by displaying its convergence history versus iterations and CPU time on three meshes of 160×80, 320×160, and 640×320 uniform cells, respectively. In those computations, $\epsilon_p = 2$.

Example 3.7 The last example simulates a steady channel flow around a hill (a relatively high bump) which is defined by

$$z(x,y) = \begin{cases} 1.2 - 0.3\left((x-10)^2 + y^2\right), & (x-10)^2 + y^2 < 4, \\ 0, & \text{otherwise}, \end{cases}$$

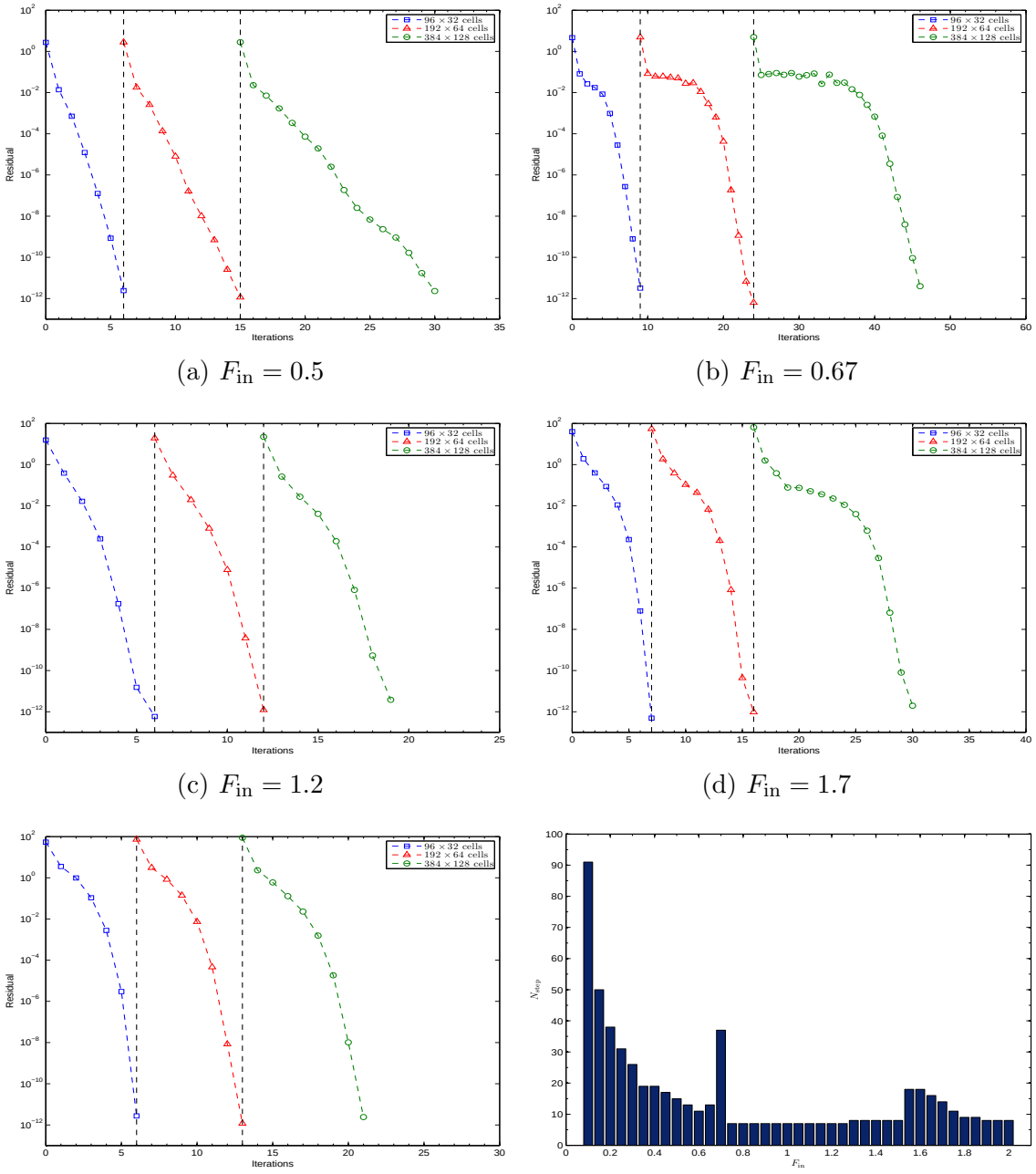

(a) $F_{\text{in}} = 0.5$ (b) $F_{\text{in}} = 0.67$

(c) $F_{\text{in}} = 1.2$ (d) $F_{\text{in}} = 1.7$

(e) $F_{\text{in}} = 2$ (f) Histogram of N_{step} versus F_{in}

Fig. 3.17. Example 3.5: (a)-(e). Convergence history in terms of the NMGM iteration number N_{step} on three meshes; (f). Histogram of the NMGM iteration number N_{step} on the mesh of 384×128 cells versus F_{in} uniformly varying from 0.1 to 2.

in the channel of $[0, 25] \times [-5, 5]$ with boundary conditions: The discharge $hu = 0.1, hv = 0$ at $x = 0$, the water height $h = 0.2$ at the downstream $x = 25$, and the reflective boundaries conditions at $y = \pm 5$ in the y–direction. Initially, the channel is full of static flow with the water height $h(x, y) = \max\{0.2 - z(x, y), 0\}$. Since the steady solution involves wet/dry transition, thus it becomes much more difficult to obtain such the steady solution by solving the time-dependent SWEs with numerical schemes. NMGM and the BLU-

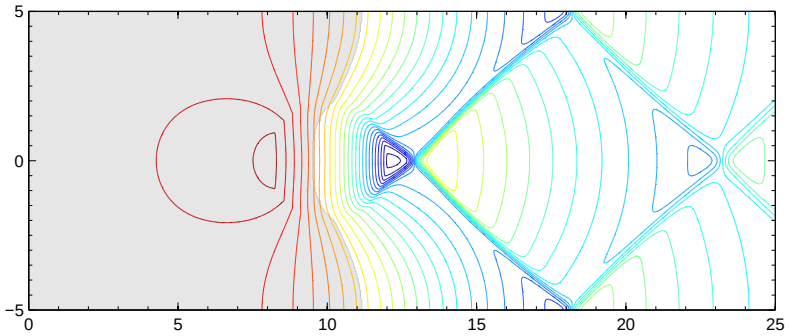

Fig. 3.18. Example 3.6: The contours of the steady water surface $h+z$ with the shaded subcritical region obtained by NMGM on the mesh of 640×320 cells. 25 equally spaced contour lines are used.

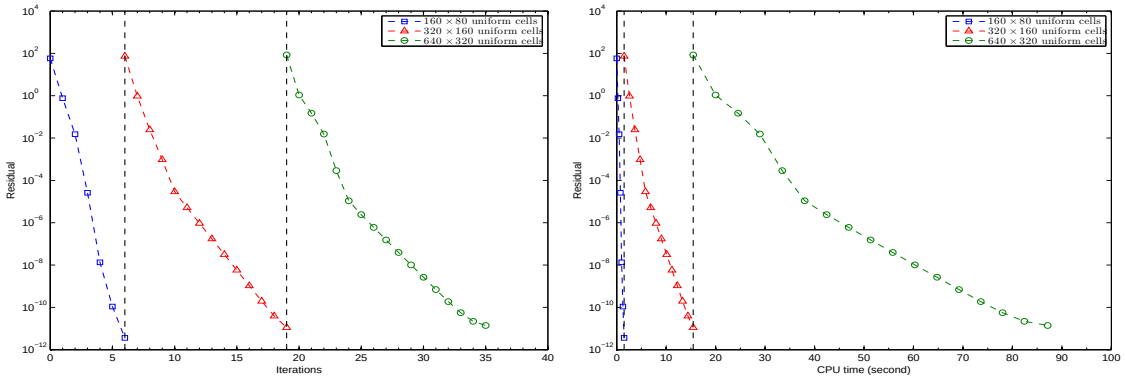

Fig. 3.19. Example 3.6: Convergence history in terms of the NMGM iteration number N_{step} (left) and CPU time (right) on three meshes.

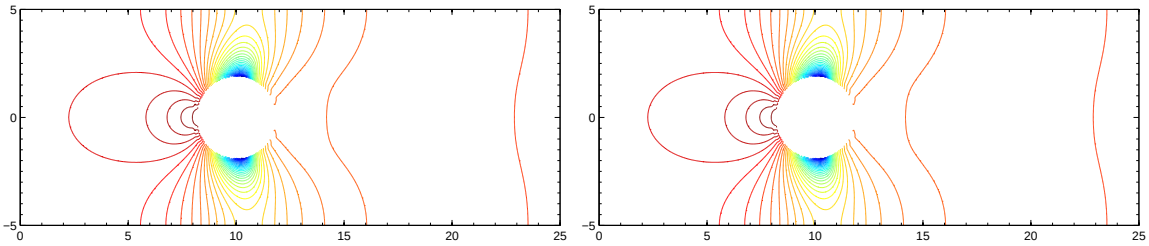

Fig. 3.20. Example 3.7: The contours of the steady water surface $h + z$ (only the wet region is shown) respectively obtained by using NMGM (left) and an explicit scheme to solve the time-dependent SWEs (right) on the mesh of 512×256 cells. 40 equally spaced contour lines from 0.1067 to 0.2201 are used.

SGS iteration with the HLLC or Roe flux fail to work.

Fig. 3.20 displays the contours of the steady water surface $h + z$ obtained by NMGM with the LLF flux on the mesh of 512×256 uniform cells, in comparison to the result given by using a first order accurate explicit finite volume scheme with LLF flux to solve the time-dependent SWEs (1.1) on the same mesh. The latter takes 412652 time steps and CPU time of 13804 seconds to reduce the residual to 1.5×10^{-12} at physical time $t = 1701.96$. The results show that the steady solution given by NMGM agree well with that given by the explicit scheme, and NMGM with the LLF flux works efficiently and robustly for the steady

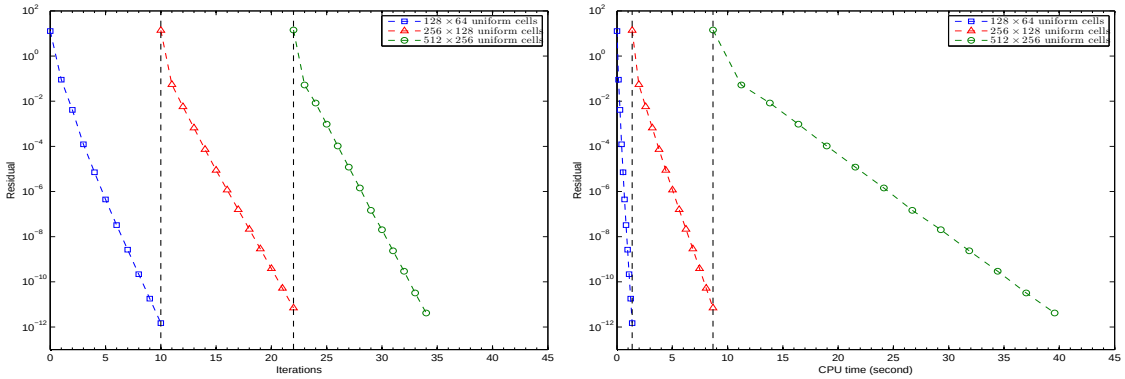

Fig. 3.21. Example 3.7: Convergence history in terms of the NMGM iteration number N_{step} (left) and CPU time (right) on three meshes.

solution with wet/dry transitions. Fig. 3.21 gives the convergence history of NMGM with LLF flux in terms of the NMGM iteration number N_{step} and CPU time on three meshes of 128×64, 256×128, and 512×256 uniform cells, respectively. It is seen that the convergence behaviors of NMGM are similar on those meshes, and N_{step} scarcely changes with the mesh refinement.

4 Conclusions

The paper developed a Newton multigrid method for 1D and 2D steady shallow water equations (SWEs) with topography and dry areas. The steady-state SWEs were first approximated by using the well-balanced finite volume discretization based on the hydrostatic reconstruction technique. The resulting nonlinear system was linearized by using Newton's method, and the geometric MG method with the block symmetric Gauss-Seidel (SGS) smoother was used to solve the linear system. The proposed Newton MG method made use of the local residual to regularize the Jacobian matrix of the Newton iteration, and could handle the steady-state problem with wet/dry transitions. Several numerical experiments were conducted to demonstrate the efficiency, robustness, and well-balanced property of the proposed method. Moreover, the relation between the convergence behavior of the proposed method with the HLL, LLF, or Roe flux and the distribution of the eigenvalues of the iteration matrix was detailedly discussed, in comparison to the block LU-SGS method. Numerical results showed that convergence behaviors of NMGM depended on the numerical flux and the Froude number of the flow.

Acknowledgements

The work was partially supported by the National Natural Science Foundation of China (Nos. 91330205 & 11421101).

References

[1] Vreugdenhil, C. B. *Numerical Methods for Shallow-Water Flow*, Springer, Dordrecht, 15–25 (1995)

[2] Glaister, P. Approximate Riemann solutions of the shallow water equations. *Journal of Hydraulic Research*, **26**, 293–306 (1988)

[3] Li, J.Q. and Chen, G.X. The generalized Riemann problem method for the shallow water equations with bottom topography. *International Journal for Numerical Methods in Engineering*, **65**, 834–862 (2006)

[4] Noelle, S., Xing, Y., and Shu, C.-W. High-order well-balanced finite volume WENO schemes for shallow water equation with moving water. *Journal of Computational Physics*, **226**, 29–58 (2007)

[5] Xing, Y. and Shu, C.-W. High order finite difference WENO schemes with the exact conservation property for the shallow water equations. *Journal of Computational Physics*, **208**, 206–227 (2005)

[6] Tang, H.Z., Tang, T., and Xu, K. A gas-kinetic scheme for shallow-water equations with source terms. Zeitschrift für angewandte Mathematik und Physik, **55**, 365–382 (2004)

[7] Xu, K. A well-balanced gas-kinetic scheme for the shallow-water equations with source terms. *Journal of Computational Physics*, **178**, 533–562 (2002)

[8] Tang, H.Z. Solution of the shallow-water equations using an adaptive moving mesh method. *International Journal for Numerical Methods in Fluids*, **44**, 789–810 (2004)

[9] Kesserwani, G. and Liang, Q. A conservative high-order discontinuous Galerkin method for the shallow water equations with arbitrary topography. *International Journal for Numerical Methods in Engineering*, **86**, 47–69 (2011)

[10] Xing, Y., Zhang, X., and Shu, C. W. Positivity-preserving high order well-balanced discontinuous Galerkin methods for the shallow water equations. *Advances in Water Resources*, **33**, 1476–1493 (2010)

[11] Bilanceri, M., Beux, F., Elmahi, I., Guillard, H., and Salvetti, M. V. Linearized implicit time-advancing and defect correction applied to sediment transport simulations. *Computers & Fluids*, **63**, 82–104 (2012)

[12] Hudson, J. *Numerical Techniques for Morphodynamic Modelling*, Dissertation, University of Reading, Reading, 1-185 (2001)

[13] Spitaleri R.M. and Corinaldesi, L. A multigrid semi-implicit finite difference method for the two dimensional shallow water equations. *International Journal for Numerical Methods in Fluids*, **25**, 1229–1240 (1997)

[14] Sármány, D., Hubbard, M. E., and Ricchiuto, M. Unconditionally stable space-time discontinuous residual distribution for shallow-water flows. *Journal of Computational Physics*, **253**, 86–113 (2013)

[15] Bagheri J. and Das, S. K. Modeling of shallow-water equations by using implicit higher-order compact scheme with application to dam-break problem. *Journal of Applied & Computational Mathematics*, **2**, 1000132 (2013)

[16] Dumbser M. and Casulli, V. A staggered semi-implicit spectral discontinuous Galerkin scheme for the shallow water equations. *Applied Mathematics and Computation*, **219**, 8057–8077 (2013)

[17] Tavellia M. and Dumbserb, M. A high order semi-implicit discontinuous Galerkin method for the two dimensional shallow water equations on staggered unstructured meshes. *Applied Mathematics and Computation*, **234**, 623–644 (2014)

[18] Glaister, P. On the efficient solution of the steady, two dimensional shallow water equations. *International Journal of Computer Mathematics*, **54**, 97–108 (1994)

[19] Chen R. F. and Wang, Z. J. Fast, block lower-upper symmetric Gauss-Seidel scheme for arbitrary grid. *AIAA Journal*, **38**, 2238–2245 (2000)

[20] Hu, G., Li, R., and Tang, T. A robust high-order residual distribution type scheme for steady Euler equations on unstructured grids. *Journal of Computational Physics*, **229**, 1681–1697 (2010)

[21] Jameson, A. Analysis and design of numerical schemes for gas dynamics 1: artificial diffusion, upwind biasing, limiters and their effect on accuracy and multigrid convergence. *International Journal of Computational Fluid Dynamics*, **4**, 171–218 (1995)

[22] Li, R., Wang, X., and Zhao, W. B. A multigrid BLU-SGS algorithm for Euler equations on unstructured grids. *Numerical Mathematics: Theory, Methods and Applications*, **1**, 92–112 (2008)

[23] Mavriplis, D. J., Jameson, A., and Martinelli, L. Multigrid solution of the Navier-Stokes equations on triangular meshes. *AIAA Journal*, **28**, 1415–1425 (1990)

[24] Audusse, E., Bouchut, F., Bristeau, M., Klein, R., and Perthame, B. A fast and stable well-balanced scheme with hydrostatic reconstruction for shallow water flows. *SIAM Journal on Scientific Computing*, **25**, 2050–2065 (2004)

[25] Liang Q. and Borthwick, A. G. L. Adaptive quadtree simulation of shallow flows with wet-dry fronts over complex topography. *Computers & Fluids*, **38**, 221-234 (2009)

[26] Toro, E. F., Spruce, M., and Speares, W. Restoration of the contact surface in the HLL Riemann solver. *Shock Waves*, **4**, 25-34 (1994)

[27] LeVeque, R. J. *Finite Volume Methods for Hyperbolic Problems*, Cambridge University Press, Cambridge, 525-531 (2002)

[28] Toro, E. F. *Shock-capturing Methods for Free-surface Shallow Flows*. John Wiley & Sons, New York, 110–114 (2001)

[29] Vazquez-Cendon, M. E. Improved treatment of source terms in upwind schemes for the shallow water equations in channels with irregular geometry. *Journal of Computational Physics*, **148**, 497–526 (1999)

[30] Delestre, O., Lucas, C., Ksinant, P. A., Darboux, F., Laguerre, C., Vo, T. N. T., James, F., and Cordier, S. SWASHES: a compilation of shallow water analytic solutions for hydraulic and environmental studies. *International Journal for Numerical Methods in Fluids*, **72**, 269–300 (2013)

[31] Zienkiewicz, O. C. and Ortiz, P. A split-characteristic based finite element model for the shallow water equations. *International Journal for Numerical Methods in Fluids*, **20**, 1061–1080 (1995)

[32] Hubbard, M. E. On the accuracy of one-dimensional models of steady converging/diverging open channel flows. *International Journal for Numerical Methods in Fluids*, **35**, 785–808 (2001)